

Investigation of Passive Safety Methods for Nuclear Reactors

by

Alexander Pegarkov

A thesis submitted to the Faculty of Graduate and Postdoctoral Affairs in

partial fulfillment of the requirements for the degree of

Master of Applied Science

in

Mechanical Engineering

Carleton University Ottawa, Ontario

©2022, Alexander Pegarkov

Abstract

Passive safety measures in nuclear reactors can reliably mitigate or prevent accident scenarios. This thesis considered two passive safety measures: plug formation and heat pipes. During a reactor core meltdown, the molten corium material can access cooling pipe connections. There is a chance that the passive plugging of melt flow due to solidification can occur, provided there is an adequate heat sink. A numerical model was created to simulate corium flow through an empty vertical pipe. The numerical model was validated through experimental work using gallium and verified using a previously built analytical model. The numerical model predicted the penetration length of gallium with an average percent error of 10.3% compared to the experimental penetration length results of gallium. The model was then modified to predict the corium penetration length during a severe nuclear accident. Numerous sensitivity studies were also conducted to better understand how certain variables impact the penetration length. Heat pipes are passive, two-phase heat exchangers with excellent heat transfer capabilities. They can be used in passive reactor core cooling and spent fuel pool cooling. Heat pipes have different operating limits that impact their operating conditions and heat transfer capabilities. A numerical approach was used to determine the operational limits of a liquid metal heat pipe that can be used in nuclear applications. The algorithms used to determine the operating limits were presented along with typical results from different operating scenarios.

Acknowledgments

Firstly, I would like to thank my supervisors, Prof. Tarik Kaya and Prof. Edgar Matida, for all their help, guidance, and support during my graduate studies. They served as true mentors to me, which helped me develop personally and put me on the proper path to achieving my future objectives.

I would like to thank my friends, Hooman Jazebizadeh, Shawn Somers-Neal, and Kaitlyn Williams, for their assistance and guidance in this research. I couldn't have accomplished this without their advice, and they were always there to support me.

I want to thank Prof. Vinh Tang for his support in my studies and research.

I want to thank my family for their endless support and patience. My father, Alexandre Pegarkov, mother, Anna Pegarkova, and brother Georgy Pegarkov encouraged me throughout my time as a graduate student and made it possible for me to achieve my dreams.

Lastly, I would like to thank the Canadian Nuclear Safety Commission (CNSC) and Canadian Nuclear Laboratories (CNL) for their technical and financial support, which made this research possible.

Table of Contents

Abstract.....	ii
Acknowledgments.....	iii
Table of Contents.....	iv
List of Tables	vii
List of Illustrations.....	viii
Nomenclature.....	xii
1 CHAPTER: Introduction	1
1.1 Research Objectives	6
1.2 Organization	8
2 CHAPTER: Literature Survey.....	9
2.1 Melt Flow Solidification	10
2.1.1 Analytical Methods	10
2.1.2 Numerical Methods.....	13
2.1.3 Experimental Methods	17
2.2 Heat Pipe in Nuclear Reactors	18

2.2.1	Nuclear Power Plant Core Thermal Control	18
2.2.2	Spent Nuclear Fuel Pool Thermal Control	20
2.3	Other Passive Safety Measures	23
3	CHAPTER: Melt Flow Solidification	26
3.1	Numerical Model.....	26
3.2	Experimental Setup	31
3.2.1	Measurement Uncertainty	34
3.3	Results and Discussion.....	36
4	CHAPTER: Operational Limits of Liquid Metal Heat Pipes	43
4.1	Mathematical Model	43
4.1.1	Heat Pipe Properties	43
4.1.2	Vapor Flow.....	49
4.1.3	Liquid Flow.....	53
4.1.4	Viscous Limit	53
4.1.5	Sonic Limit.....	55
4.1.6	Capillary Limit	58

4.1.7	Entrainment and Flooding Limit.....	61
4.1.8	Boiling Limit.....	64
4.2	Solution Procedure.....	65
4.2.1	Working Fluid Property Calculation.....	67
4.2.2	Viscous Limit.....	68
4.2.3	Sonic Limit.....	71
4.2.4	Capillary Limit.....	81
4.2.5	Entrainment and Flooding Limit.....	87
4.2.6	Boiling Limit.....	92
4.3	Results.....	94
5	CHAPTER: Conclusions.....	100
5.1	Future Work.....	102
	Publications.....	104
	References.....	105

List of Tables

Table 1: Experimental results for gallium, where V is the velocity, Re is the Reynolds number, and Xp is the penetration length.	36
Table 2: Vapor frictional term for different flow cases [43]	60

List of Illustrations

Figure 1: Schematic of pressurized water reactor [2].	2
Figure 2: Model concept of reactor vessel assembly [4].	4
Figure 3: Schematic of the corium solidification in pipe [4].	4
Figure 4: Heat pipe schematic.....	5
Figure 5: Comparison of experimental data with Epstein equation (dashed line) [7]	11
Figure 6: Schematic of physical configuration for freezing penetration of moving fluid in a channel [8]......	12
Figure 7: Schematic of CANDU 6 core [14].	15
Figure 8: CANDU primary heat transport system (1. steam line leading to turbines, 2. pressurizer, 3. steam generator, 4. pumps, 5. inlet headers, 6. calandria vessel, 7. fuel channel, 8. moderator circulation pump, 9. moderator heat exchanger, and 10. online refueling machines) [14].	16
Figure 9: Schematic of proposed heat pipe ECCS with gravity-assisted feed water system [18].	19
Figure 10: Schematic of the FEHP in a spent fuel pool [28]......	21
Figure 11: Sketch of the vertical pipe flow.....	29
Figure 12: Sketch and photograph of the experimental setup.....	32

Figure 13: Comparison of the numerical, analytical, and experimental results for penetration length vs. Reynolds number.....	37
Figure 14: Comparison of leading node velocity vs. penetration length of gallium at different Reynolds numbers.....	39
Figure 15: Comparison of penetration length of gallium vs. Reynolds number at different pipe diameters.	40
Figure 16: Comparison of penetration length of corium vs. Reynolds number at different pipe diameters.	41
Figure 17: Radius of liquid corium vs. the penetration distance in the pipe for three different Reynolds numbers.....	42
Figure 18: Wick structure schematic: (a) screen mesh, (b) annular-gap mesh, and (c) arterial mesh [40]......	45
Figure 19: Numerical model algorithm.....	67
Figure 20: Busse option 1,2,3	69
Figure 21: Simple iterative algorithm	70
Figure 22: Simple iterative algorithm with Fanno flow.....	71
Figure 23: Levy methods and Busse method	72
Figure 24: Iterative Mach number algorithm.....	74

Figure 25: Iterative power method 1.....	76
Figure 26: Iterative power method 2.....	78
Figure 27: Iterative power method 3.....	80
Figure 28: Reay & Kew algorithm.....	81
Figure 29: Simplified Chi algorithm.....	82
Figure 30: Chi algorithm.....	84
Figure 31: Iterative pressure method	86
Figure 32: Faghri, Sterbentz, Reay & Kew algorithm	87
Figure 33: Prenger algorithm	88
Figure 34: Iterative power method.....	89
Figure 35: Iterative temperature method.....	91
Figure 36: Flooding limit method.....	92
Figure 37: Faghri algorithm.....	93
Figure 38: Reay & Kew algorithm.....	94
Figure 39: Numerical model comparison (a) Dickinson model [40] (b) our model.....	95
Figure 40: Viscous limit comparison.....	96

Figure 41: Sonic limit comparison.....	97
Figure 42: Capillary limit comparison.....	98
Figure 43: Entrainment limit comparison.....	98
Figure 44: Boiling limit comparison.....	99
Figure 45: Operational envelope of possible CNL potassium heat pipe.....	100

Nomenclature

A	Area [m^2]
a	Sonic velocity/speed of sound [m/s]
B	Bias Error
Bo	Bond number
C_k	Constant
cma	Compressibility factor
D	Diameter [m]
d	Distance [m]
e	Euler's number
f	Fanning friction factor
FF	Fanno flow factor
F	Pressure drop factor
G	Minimum to maximum vapor pressure ratio
g	Gravitational acceleration [m/s^2]
h	Specific enthalpy [J/kg]
h_{fg}	Specific latent heat [J/kg]
K	Loss coefficient, Thermal conductivity [W/mK]
L	Length [m]
M	Mach number
\dot{m}	Mass flow rate [kg/s]
N_{mesh}	Number of mesh [$1/\text{m}$]
P	Pressure [Pa]
Pr	Pressure ratio
\dot{Q}	Rate of heat transfer or heat load [W]
R	Specific gas constant [J/kgK]
r	Radius [m]
Re	Reynolds number
S	Random error
T	Temperature [K]
t	Time[s] and Thickness [m]
U	Internal Energy [J]
U_{x_p}	Uncertainty
u	Velocity [m/s]
V	Velocity [m/s]
We	Weber number
x_p	Penetration distance/length [m]
z	Wick inner surface characteristic length [m]
z_{fixed}	Gallium height in reservoir [m]
Greek symbols	
β	Compressibility

ε	Surface roughness
σ	Surface tension [Pa m]
θ	Tilt angle [$^{\circ}$], positive when the evaporator is below the condenser
δ	Thickness or depth [m]
μ	Dynamic viscosity [Pa s]
κ	Permeability [m ²]
ρ	Density [kg/m ³]
τ	Shear stress [N]
γ	The ratio of specific heats
φ	Porosity
Subscripts	
0	Stagnation point
<i>a</i>	Adiabatic
<i>arty</i>	Artery
<i>b</i>	Bubbles, Bulk
<i>boi</i>	Boiling
<i>c, cond</i>	Condenser
<i>cap</i>	Capillary
<i>cri</i>	Critical
<i>cv</i>	Control volume
<i>e, evap</i>	Exit, Evaporator
<i>eff, t</i>	Total effective
<i>eff, s</i>	Total powered effective
<i>ent</i>	Entrainment
<i>exit</i>	Exit
<i>flo</i>	Flooding
<i>g</i>	Gravity
<i>gap</i>	Gap
<i>hyd</i>	Hydraulic
<i>i</i>	Inlet, Inertia
<i>in</i>	Inner
<i>inlet</i>	Inlet
<i>isentropic</i>	Isentropic
<i>isothermal</i>	Isothermal
<i>l</i>	Liquid
<i>layr</i>	Layer
<i>men</i>	Meniscus
<i>mesh</i>	Mesh
<i>out</i>	Out
<i>son</i>	Sonic
<i>tota</i>	Total
<i>tb</i>	Thermal boundary layer
<i>v, vap</i>	Vapor

<i>vis</i>	Viscous
<i>w, wick</i>	Wick
<i>wall</i>	Wall
<i>wire</i>	Wire
X_p	Penetration length
Superscripts	
t	Current time-step
$t + \Delta t$	Next time-step
*	Reference (for thickness)

1 CHAPTER: Introduction

An earthquake struck Japan on March 11, 2011 [1]. Two tsunami waves that followed the earthquake led to an area-wide power outage. As a result, the Fukushima Daiichi Nuclear Power Plant experienced power outages and had to start using backup generators in some of the basements of nearby structures to keep running. The backup generators, seawater cooling pumps, residual heat removal system, and electrical switchgear necessary to operate each reactor were all housed in basements that were swamped by tsunami waves. The reactor systems heated up and started to melt since no water was being pumped to cool them. The excessive steam pressure and the presence of hydrogen gas triggered numerous explosions in the reactor [1]. Two individuals died because of this catastrophe, thousands of people had to be relocated, and it had billions of dollars in repercussions on the environment and the people it affected.

Improving the safety measures of reactors has been an active research field. The Fukushima accident made it clear that passive safety systems are more desirable in case of an accident. Two passive methods of interest include molten metal penetration and solidification in vertical pipes and the use of heat pipes, more specifically Liquid Metal Heat Pipes (LMHPs), for thermal control of a nuclear reactor core and spent fuel pools.

It is essential to understand how nuclear fission reactors work. Electricity is produced by nuclear fission reactors using isotopes of elements like uranium-235 and plutonium-239 [2]. Isotopes are separated into smaller pieces by a process called fission. Large amounts of thermal energy are released during this process, and power reactors can utilize that energy to produce electricity. To prevent an unnecessarily high rise in reactor temperature, the energy released by

fission must be continuously withdrawn. Three subsequent loops in pressurized water reactors remove this energy under typical operating conditions. Figure 1 shows the first loop, the reactor coolant system, which circulates water through the core to cool it. The second loop takes heat from the reactor coolant system and uses it for the steam generators. The heat creates steam which is used in the turbine generators to generate power. The last loop consists of a condenser that rejects any remaining heat from the turbines to an environment nearby, such as the atmosphere or a river.

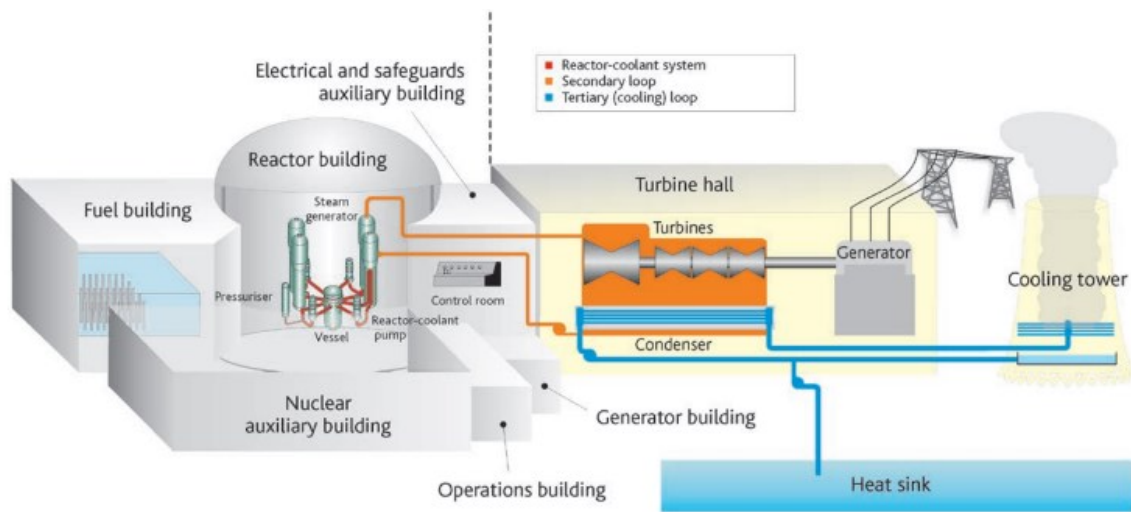


Figure 1: Schematic of pressurized water reactor [2].

In pressurized water nuclear reactors, a Loss of Coolant Accident (LOCA) can happen when the cooling system's pipework is compromised [2]. Steam would start to accumulate in the nuclear core because of inadequate cooling. When zirconium material reacts with the hot steam within a reactor, hydrogen gas can be released, creating an explosive atmosphere. When a steam generator's feedwater line ruptures, a "steam-line break" accident may result [2]. Without water flowing into the steam generator, the secondary side of the generator's steam flow rate would increase, increasing the heat removed from the reactor coolant system. The impact of this cooling would reduce the available reactivity shutdown margin and would automatically initiate a reactor

trip. If several control rods do not function as required or become stuck outside the core, or if the break in the line is not isolated, a core meltdown may occur. The core would start to melt if the situation cannot be handled with sufficient residual heat removal. As a result, the nuclear reactor site may experience a power outage or station blackout. As a result, the feedwater and the reactor coolant system would not operate correctly. The system's temperature would rise, and core melt might happen. In-vessel retention is a passive safety mechanism created in response to basement melt penetration (BMP), the primary safety issue of numerous reactors [3]. BMP is primarily concerned with the possibility of corium accumulating at the base of the reactor pressure vessel. Corium is a lava-like substance consisting of fission products, nuclear fuel, support structures, and other components that can melt and mix during a meltdown.

A visual representation of a reactor pressure vessel assembly can be seen in Figure 2. If enough corium builds up at the bottom of the tank, it could overflow into pipes or other equipment connected to the reactor pressure vessel. The corium could then passively harden and stop the spread of the molten material, provided that there is appropriate cooling surrounding the attached pipes or devices to remove the stored heat in the corium. Therefore, it is crucial to model the melt flow penetration length and the solidification process in pipes to better understand if passive containment of the molten radioactive material is possible. This passive safety measure is experimentally and numerically studied in this thesis.

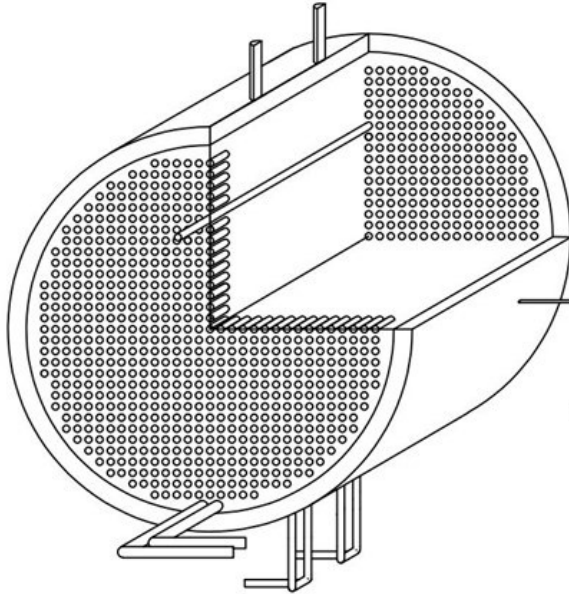


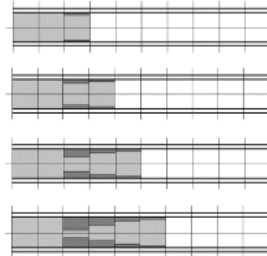
Figure 2: Model concept of reactor vessel assembly [4].

A visual illustration of corium penetrating a pipe is shown in Figure 3.

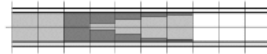
Time marching (light grey is liquid metal, and dark grey is solid metal):



Solidification temperature is reached:



Plugging occurs:



Freezing/Plugging
Location

Penetration Length

Figure 3: Schematic of the corium solidification in pipe [4].

The second passive safety measure studied in his thesis is based on the use of heat pipes. A heat pipe is a two-phase heat transfer device with a working fluid circulating between an evaporator and condenser [5]. Heat pipes are used to enhance the thermal performance of heat exchangers in microelectronics, air conditioning systems, spacecraft, air conditioning systems, and different nuclear reactor technologies. A typical heat pipe is a self-contained device that uses capillary forces and two-phase fluid flow to achieve extremely high thermal conductivity [5]. The condenser section is exposed to a heat sink while the heat is applied to the evaporator section. At the evaporator, energy is transmitted into the working fluid, causing it to evaporate. To reach the condenser, this vapor passes through an adiabatic section. In the condenser, the vapor condenses and releases energy. Figure 4 shows a schematic of a typical heat pipe that demonstrates this procedure.

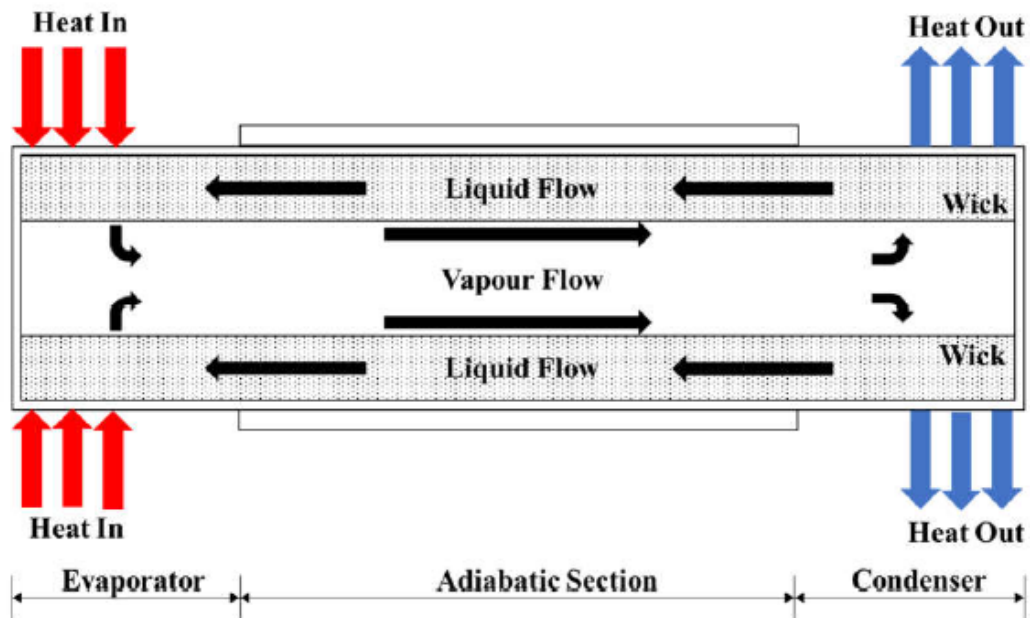


Figure 4: Heat pipe schematic.

Heat pipes utilize a wick structure to promote the flow of liquid from the condenser to the evaporator because of the surface tension forces formed on the inner surface of the wick. Heat pipes can be employed in microgravity situations and in various orientations, such as horizontal, gravity-assisted (evaporator below condenser), and adverse gravity, thanks to the wicking structure that encourages the circulation of the working fluid (evaporator above condenser).

A more dependable and secure means of cooling nuclear reactors has always been required. The best solid metallic conductors cannot compare to the thermal conductance of liquid metal heat pipes, which is thousands or even tens of thousands of times better [5]. When compared to heat exchange by a geometrically equivalent system, heat pipes may transport significantly more heat through latent heat, making them ideal for nuclear reactor applications [5]. Since surface tension forces and the high vapor pressure in the evaporator drive the working fluid circulation, mechanical pumping systems are not required. Heat pipes can function in a wide range of temperatures while retaining high efficiency and being relatively light compared to the rest of the system, depending on the working fluid chosen. Due to these factors, heat pipes have been suggested and thoroughly investigated as a potential passive cooling option for different types of nuclear reactors in both regular operation and accident scenarios. Heat pipes are also optimal passive cooling options for spent fuel pools.

1.1 Research Objectives

The purpose of this research is to gain a better understanding of two passive safety methods for nuclear reactors. The first one is molten flow and possible solidification in vertical drainpipes that are initially empty. The second is the use of liquid metal heat pipes for reactor core and spent fuel pool thermal control. To accomplish this, both computational and experimental techniques

will be used. The numerical models will be developed and validated using the findings of the experiments and previous research findings.

The following milestones were accomplished to reach the research objective:

Molten flow solidification:

- Conducted a literature review on the molten flow and solidification of fluids to better understand the body of literature encompassing analytical, numerical, and experimental work.
- Built an experimental setup to perform various tests on the solidification of gallium metal flow in a vertical pipe.
- Updated a numerical 1-D model to simulate the molten flow and solidification process in a vertical pipe.
- Updated the numerical model for corium using the results of the experimental tests.
- Conducted numerous simulations to better comprehend the flow and possibility for corium solidification in vertical pipes.

Heat pipes:

- Performed a literature survey on the use of heat pipes in the nuclear reactor core and spent fuel pool thermal control, including an investigation of common heat pipe limitations.
- Developed a numerical model to optimize the operating envelope of a liquid metal heat pipe with various internal structures and compositions.

With the goal of the research established, the organization of the thesis can be discussed as follows.

1.2 Organization

The organization of the thesis is discussed in this section. The thesis includes five chapters, which are organized in the following format.

- Chapter 1 – Introduction: Introduces the background information on the importance of passive safety measures in nuclear reactors, outlines the research objectives, and the organization of the thesis.
- Chapter 2 – Literature Survey: Summarizes the existing literature on analytical, numerical, and experimental solidification of liquids in pipe flow. Also, summarizes the current literature on the use of heat pipes for nuclear reactor core and spent fuel pool thermal control.
- Chapter 3 – Melt Flow Solidification: The corium and gallium numerical model is described. The fundamental equations, presumptions, and schemes are thoroughly presented, along with the differences between the two materials and the verification procedure. The design of the experimental setup and significant results are also discussed.
- Chapter 4 – Operational Limits of Liquid Metal Heat Pipes: All possible heat pipe limitations and the numerous methods of obtaining them are presented. The numerical model and its algorithms used to optimize the operating envelope of a potassium metal heat pipe are explained in detail.
- Chapter 5 – Conclusion: Discussion of the key findings together with suggestions for further development are presented.

2 CHAPTER: Literature Survey

Essential safety functions in nuclear reactors are used to control reactivity, cool the fuel, and contain radioactive substances [6]. Typical reactors use control rods to absorb neutrons, thus regulating the fission process. Emergency core cooling systems are used to remove excess heat and contain the reactor in a severe accident scenario. These safety measures involve active machines like diesel generators, pumps, and valves. The use of passive safety measures that do not have moving mechanical parts can decrease the chances of equipment failure or operator error from occurring.

Passive safety measures in nuclear reactors are not fully understood as past and current reactor designs do not use passive safety features. The core of a power plant can melt during a severe nuclear reactor accident [2]. The resulting mixture of molten nuclear fuel and other in-core materials is known as corium. The corium has the potential to flow through connecting piping and other penetrations in the nuclear plant.

Heat pipes have recently been considered as a potential passive nuclear reactor heat exchanger. A heat pipe is a two-phase heat transfer device with a working fluid circulating between an evaporator and condenser [5]. Heat pipes are used to improve the thermal performance of heat exchangers in microelectronics, air conditioning systems, spacecraft, and numerous nuclear reactor technologies. Heat pipes have been proposed as a passive nuclear core and spent fuel pool heat removal system.

Liquid metal heat pipes can provide passive hands-off thermal control of nuclear reactors during operation, but if a reactor accident is to occur passive solidification of corium in different piping systems may contain the spread of radioactive material to the surrounding environment.

2.1 Melt Flow Solidification

Previous research in melt flow solidification can be categorized into the following methods: analytical, numerical, or experimental. It is important to note that the majority of these studies were performed using materials that are not optimal for modeling corium which is a mixture of ceramics and metallic compounds.

2.1.1 Analytical Methods

Epstein et al. [7] proposed a model that approximated freezing water penetration within a cold tube. In this model, the flow was considered to be turbulent, and the solid-to-liquid interface was assumed to be at a constant temperature. Furthermore, the friction factor was estimated using the Blasius equation. Assumptions were made to neglect the conduction that would occur in the flow direction, along with neglecting the thermal resistance of the tube wall. The pressure loss in the entrance region was also ignored. Another assumption included considering the physical properties of the working fluid to be constant. The final analytical model produced a non-dimensional expression to predict the penetration length of a liquid. This model tended to under-predict the penetration length when compared to experimental results [7]. Figure 5 compares the Epstein equation (dashed line) to several experimental tests.

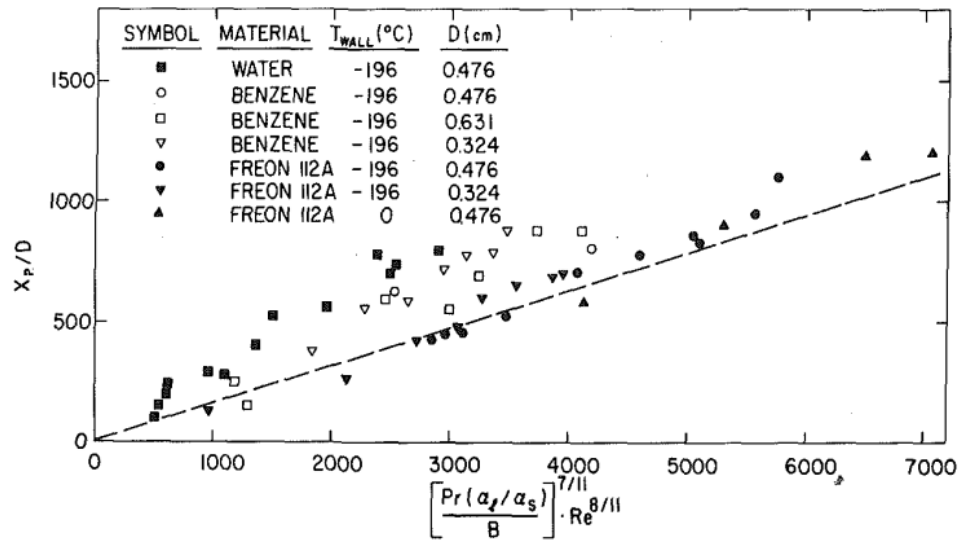


Figure 5: Comparison of experimental data with Epstein equation (dashed line) [7]

A model created by Best et al. [8] focused on a pressure-driven turbulent pipe flow without considering the effects of gravity. They assumed the pipe wall material would melt as the molten corium was freezing. They showed the freezing behavior of corium and determined the penetration distance of corium flowing in a channel. They predicted a loss of thousands of kilograms of corium if the corium escaped the reactor vessel and penetrated empty drainpipes [8]. The Best et al. model also included a crust rupture mechanism, which allowed them to predict when and where a crust would form in the flow and then rupture to cause further penetration. The model also predicted the time and location of steel entrainment after the steel pipe melted and mixed with corium. The model made numerous significant assumptions to derive the essential equations used in the model. They assumed the flow to be one-dimensional and incompressible with constant physical properties [8]. The solid-liquid interface temperature was considered to be equal to the material equilibrium solidification temperature, and the liquid injection pressure was sufficiently high to

$$f_o = \frac{0.316}{Re^{1/4}} \quad 4000 < Re < 10^5 \quad (1)$$

Furthermore, the fluid level in the reservoir was assumed to be constant. The gravitational pressure gains/losses and entrance losses were assumed negligible. The axial conduction was assumed to be due to a thin crust layer, and the molten fuel was at its melting temperature. The wetted perimeter was considered constant to simplify the freezing problem. The reservoir pressure was assumed to impact the stagnant molten wall structure, specifically the molten length and the channel inlet mouth. All the assumptions listed were used to determine a final penetration distance expression, as shown below in Eq. (2) [8].

$$x_p = \frac{D_o}{4f_o} \left[\left(\frac{2f_o u_o t_c}{D_o} + 1 \right)^{2/3} - 1 \right] \quad (2)$$

where x_p represents the penetration distance (m), D_o represents the hydraulic diameter (m), U_o the initial velocity (m/s), t_c the time at which the crust growth would fill the channel (s), and f_o represents the Blasius friction factor evaluated at initial conditions.

2.1.2 Numerical Methods

A numerical model created by Sampson and Gibson focused on molten metal freezing in pipe flow for both laminar and turbulent flow regimes [10], [11], [12]. The laminar model predicted whether blockage would occur in a pipe or not. The model showed acceptable agreement with the experimental results. The turbulent model was created in a similar method to that of the laminar model. The turbulent model also incorporated the use of liquid metals as the working fluid. The authors concluded that the model reasonably described the solidification layer. Nonetheless, the

authors found that a more refined model would be required for cases where a blockage would occur since the presence of a mushy region, which does not behave as a Newtonian fluid, would make the problem considerably more complex.

Barron et al. [13] studied the solidification process of molten iron in a pipe using commercial software. The objective was to solve a 3D transient simulation of molten iron in a pipe flow using ANSYS Fluent. A Reynolds Stress Model (RSM) turbulence model was chosen. The authors concluded that the pipe wall temperature was a critical factor in the solidification and blocking phenomena for molten-metal pipe flow. Therefore, the pipe wall temperature must be carefully considered during molten-metal pipe flow scenarios.

For applying molten-metal pipe flow as a safety feature to nuclear reactors, specifically for the Canadian Deuterium Uranium (CANDU) reactor, several numerical computational codes have been developed to evaluate severe accident scenarios. A handful of these codes are MAAP-CANDU, ISAAC, SEVAX, RELAP/SCDAP, MELCOOL, and ASTEC [14]. These codes focus on the calandria vessel and are used to evaluate the progression of an accident and estimate possible source terms that may contribute to an accident situation. Figure 7 shows a schematic of the fuel channels in the calandria vessel of a CANDU 6 reactor core.

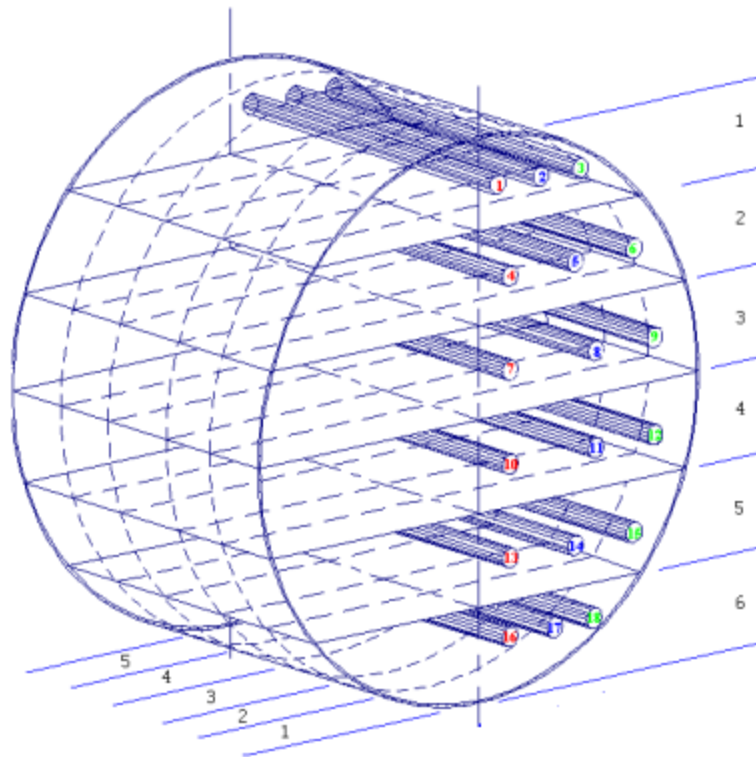


Figure 7: Schematic of CANDU 6 core [14].

MAAP is a vital modeling tool used to analyze nuclear plants, and the MAAP4-CANDU can simulate the response of the CANDU power plant during a severe accident. The code predicts the evolution of an extreme accident scenarios starting from full power conditions, including core melt, primary heat transport system failure, calandria tank failure, shield tank failure, and containment failure [14]. The code can predict the actions required to stop the accident by cooling debris in the calandria tank or containment vessel. The thermal-hydraulics, fission product behavior in the primary heat transport system, steam generator and pressurizer in Loops 1 and 2, calandria tank, shield tank, containment, and vacuum building are also modeled in the code. A schematic of the CANDU primary heat transport system can be seen in Figure 8.

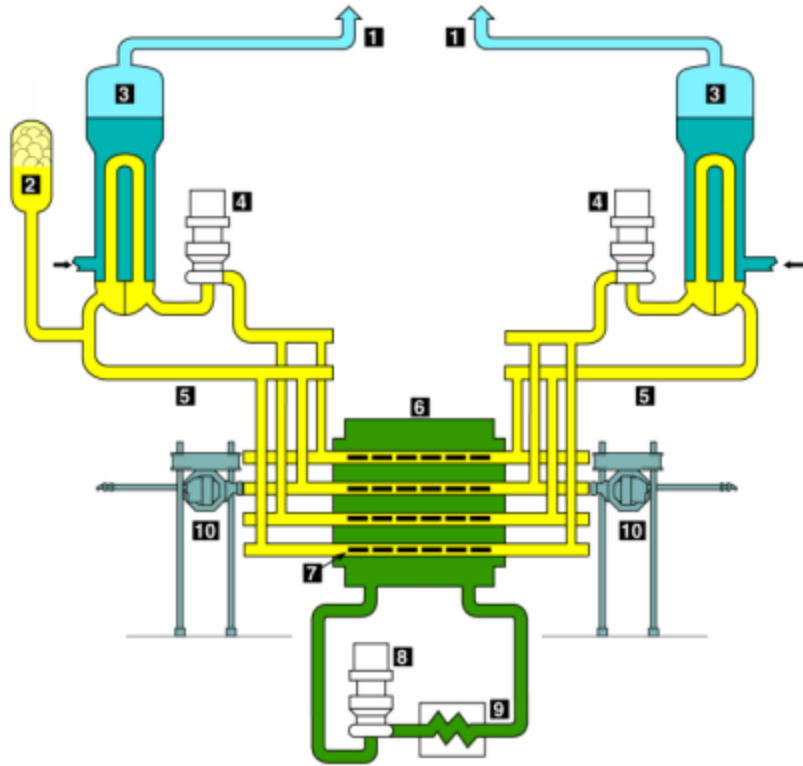


Figure 8: CANDU primary heat transport system (1. steam line leading to turbines, 2. pressurizer, 3. steam generator, 4. pumps, 5. inlet headers, 6. calandria vessel, 7. fuel channel, 8. moderator circulation pump, 9. moderator heat exchanger, and 10. online refueling machines) [14].

A more recent code called ROSHNI is an integrated numerical simulation package that models risk-sensitive core components and fluids along with relevant thermo-physical-chemical phenomena for severe accidents in Pressurized Heavy-Water Reactors (PHWR) [15]. This code improves on previous ones by considering new and different reactor features and modeling various failure mechanisms. The code also considers new accident progression pathways, detailed heavy water properties, and containment modeling. Previous research emphasizes that the available codes have been good representations based on the requirements of older generation technology. Still, they do not meet today's requirements, and thus updates need to be introduced.

2.1.3 Experimental Methods

Zerkle and Sunderland [16] conducted experiments to study liquid solidification in a circular tube with laminar flow in the thermal entrance region using water. They found that their experimental pressure drop data disagreed with their analytical value by 150%. They concluded that these differences must be due to neglecting the influence of free convective heat transfer. The experimental results presented by Zerkle and Sunderland were used as the benchmark for many future experimental works on liquid-flow solidification in circular tubes.

Spencer and Quastel [17] conducted experimental work on the formation of corium plugs in an externally cooled curved vertical pipe. They used a prototypic CANDU corium produced through a thermite reaction [17]. The objective of the experimental work was to collect data on corium flow and freezing plug formation while developing possible experimental procedures and techniques. One of the tests resulted in no penetration, which the authors hypothesized may have been due to the use of a specific sheet of stainless steel that was thick enough to allow for the formation of a thin crust on its surface before it was melted. Another test was more successful; the penetration distance was approximately 400 mm, which was in close agreement with an analytical model where the penetration distance was predicted to be 364 mm. Transient dry-out and boiling behaviors on the outer surface of the pipe were observed visually and through temperature measurements [17]. They stated that future experimental work should include larger masses of melt material to reduce the cooling rate following the thermite reaction. This would allow for a reduction in uncertainty with respect to initial conditions. Additionally, using an active valve would help avoid premature material relocation, leading to a continued exothermic reaction within the pipe.

2.2 Heat Pipe in Nuclear Reactors

Previous research on the use of heat pipes in nuclear reactors is vast. This thesis focused on two areas of significant value: thermal control of the nuclear reactor core and thermal management of spent fuel.

2.2.1 Nuclear Power Plant Core Thermal Control

Suppose a severe accident occurs such that the electrical power supply to run the active cooling system of nuclear reactors is lost. In that case, a nuclear reactor containment vessel melt may occur along with other catastrophic scenarios such as a core explosion. Mochizuki et al. [18] proposed a passive cooling system, Emergency Core Cooling System (ECCS), using loop heat pipes to cool the residual heat of nuclear reactors in an emergency. The proposed loop heat pipe is composed of a cylindrical evaporator with 62 vertical tubes, each 150 mm in diameter and 6 m in length, mounted around the circumference of the nuclear fuel assembly. A naturally cooled finned condenser with a length of 21 m is installed outside the primary containment. It was claimed that the loop heat pipe could reduce the reactor temperature from 282 °C to below 250 °C within 7 hours. The proposed design can be seen in Figure 9.

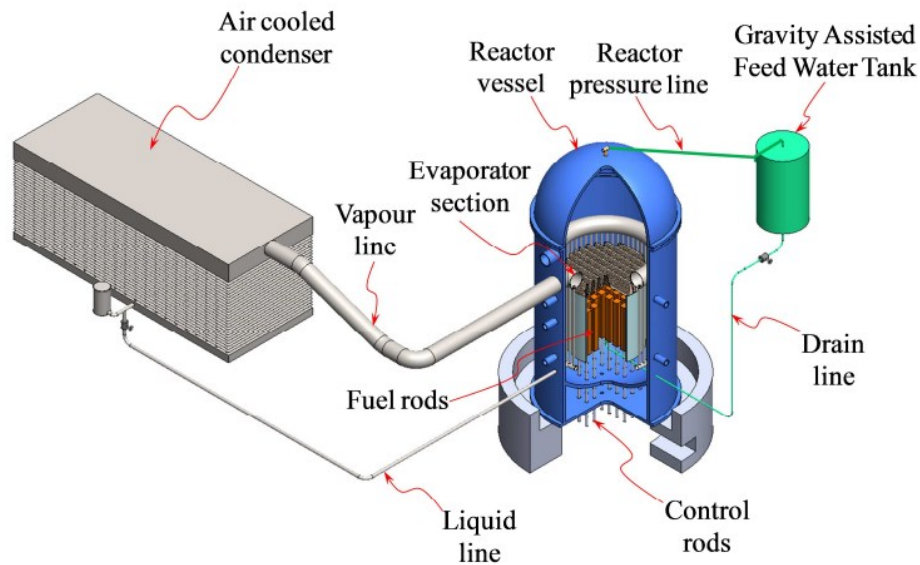


Figure 9: Schematic of proposed heat pipe ECCS with gravity-assisted feed water system [18].

The ECCS also includes an elevated feed water tank which would flood the core during an accident to accelerate the cooling of the core and replenish coolant during a loss of coolant accident (LOCA). The loop heat pipe would operate in an entirely passive mode with high runtime reliability, providing a safer environment for a nuclear power plant. To validate the concept, a water-charged loop heat pipe prototype was manufactured and tested [18].

The Atomic Energy of Canada Limited (AECL) developed a nuclear reactor called the “Nuclear Battery.” The primary reactor cooling system consisted of a liquid-metal potassium heat pipe [19]. The design included 159 heat pipes regularly dispersed throughout the fuel lattice, consisting of a sealed metal tube 5 cm in diameter and 3 m long. The top of the heat pipe protruded above the reactor core. The heat pipe had a thin wall thickness and was constructed from a niobium alloy. A screen-mesh wick structure lined the pipe's interior and distributed the liquid metal potassium working fluid uniformly.

A design called the Heat Pipe-Operated Mars Exploration Reactor (HOMER) was proposed by Poston [20]. This reactor was designed especially for producing electricity on the surface of Mars. It used sodium heat pipes to transfer heat from the reactor core to a power conversion unit, a Stirling engine. The HOMER was designed to be a near-term, low-cost system that used existing technology to simplify the system and maximize testing. A similar design was presented by Bushman et al., where lithium heat pipes were used to transfer heat to a power conversion system and to cool the reactor core of the Martian Surface Reactor (MSR) [21].

Dulera and Sinha [22] proposed to use sodium heat pipes to passively transfer heat from the upper plenum to the heat utilization vessels in a high-temperature reactor. Wang et al. proposed a passive residual heat removal system (PRHRS) design using a sodium-potassium liquid metal heat pipe for a molten salt reactor [23]. A Scalable Liquid Metal cooled small Modular reactor (SLIMM) was proposed by El-Genk and Palomino [24]. This design used liquid-metal heat pipes to transfer waste heat from the primary heat generating vessel to an electricity generating system. Two 5-MW Special Purpose Reactor (SPR) designs utilizing liquid-metal heat pipes for passive cooling were presented by Sterbentz et al. [25]. Yao et al. [26] presented a Mars surface nuclear reactor system design that used potassium and lithium heat pipes for passive reactor cooling. Mueller and Tsvetkov [27] gave a novel integrated design of Fuel Elements and Heat Pipes (FEHP) to cool a nuclear reactor core passively. This design has a variable cross-sectional area to accommodate a reactor fuel element inside the heat pipe evaporator.

2.2.2 Spent Nuclear Fuel Pool Thermal Control

During a nuclear accident where a station blackout may occur, active cooling of spent nuclear fuel water pools using pumps is no longer possible [28]. The water within the pool would

heat up due to the decay heat from the spent fuels, and then evaporation would occur, resulting in the fuel being exposed to air. Hydrogen gas would be produced due to oxidation of the zircaloy cladding, resulting in the accumulation of hydrogen gas which would be harmful if detonation occurred. Choi et al. proposed a new concept of a gravity-assisted heat pipe that removes spent fuel decay heat in the water pool by natural convection with ambient air [28]. The design was called a fork-end heat pipe (FEHP). An illustration of this heat pipe can be seen in Figure 10.

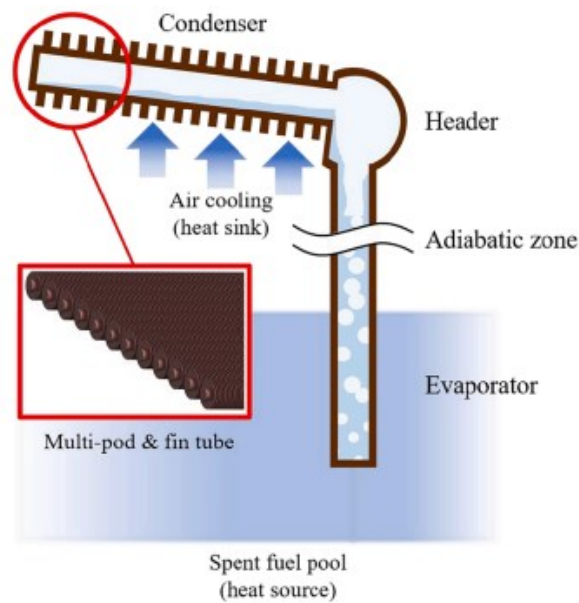


Figure 10: Schematic of the FEHP in a spent fuel pool [28].

This design consists of a condenser at the top of the heat pipe with several finned tubes for passive air cooling. The evaporator is at the bottom, which is submerged in the spent fuel pool. A theoretical analysis model was developed to validate the design, and a laboratory-scale specimen was manufactured and tested. It was concluded that the theoretical analysis model reasonably predicted the heat transfer rate of the FEHP specimen at different operating conditions. The operating limit point was predicted due to the counter-current flow limit.

Kusuma et al. conducted an experimental investigation of a vertical, straight, and wickless heat pipe 6 meters in height. They compared the results with those from a simulation done with nuclear reactor thermal-hydraulic code RELAP5/MOD3.2 [29]. The condenser in the experimental specimen was placed in a jacket and cooled by forced convection. The heat removal amount at the condenser was measured along with the temperature at the outer wall of the heat pipe and the internal pressure. Parametric studies were also performed on the heat pipe. The working fluid filling ratio, evaporator heat load, and coolant flow rate of the water jacket were examined as a function of the heat pipe pressure. Based on the heat pipe thermal performance results, they concluded that the heat pipe could be used as a passive cooling system in nuclear-spent fuel pools.

A design of a Passive Cooling System with a Closed-Loop Heat Pipe (PCSHP) was proposed by Lu et al. [30]. They tested the proposed design using computational methods and testing. The experimental conditions were divided into the start-up, steady-state, and decay heat simulation conditions. The experimental results were compared to numerical results using the Generation of Thermal Hydraulic Information for Containment (GOTHIC) code. They demonstrated that the pressure changes in the containment vessel, the flow rates, pressure, and temperature changes in the heat pipe loops were all reasonably accurate.

Ye et al. proposed a conceptual design of a spent-fuel-pool passive cooling system with a loop heat pipe for the Chinese Advanced Reactor 1400 (CAP1400) [31]. The evaporator of the heat pipe was placed into the spent fuel pool, which would heat the water working fluid inside the heat pipe. The water would evaporate and flow upwards to the condenser in an external cooling tower at a higher elevation than the pool. The vapor would then condense to liquid and return to the evaporator by gravity. The cooling system's ability to remove the spent-fuel decay heat was

evaluated using an ANSYS Fluent simulation. The simulation results showed that the passive cooling system effectively removes the decay heat from the spent-fuel storage pool that has been in storage for 15 years and prevents the burnout of the fuel rods [31]. The feasibility of water use was also demonstrated since the results showed it would not boil even during a severe accident, where emergency power and outside assistance are lacking. Work was later done by Xiong et al. [32], who manufactured a prototype of a single loop heat pipe specimen based on Ye et al. design. Experimental work was done to determine the heat pipe prototype's heat transfer performance. The results showed that up to 10.5 kW of heat could be removed by the heat pipe made of one evaporator and condenser at normal operating conditions. Parametric studies on the heat pipe showed that the heat transfer rate is most sensitive to the heat source temperature.

2.3 Other Passive Safety Measures

In addition to the passive safety measure presented above, various alternative passive systems have been researched in the past and even implemented in current operating nuclear reactors. Westinghouse Electric Company has implemented a handful of these safety measures in a Generation III+ reactor called the AP1000. Recent research is being done on the Generation IV reactors, which involve many possible safety systems.

The AP1000 Reactor design is a two-loop Pressurized Water Reactor (PWR) with passive safety features and extensive design improvements that enhance the reactor's construction, operation, maintenance, and safety [33]. The passive safety measures in the design maintain core cooling and containment integrity indefinitely, with no operator or AC power support requirements. The safety systems are substantially simpler than typical PWR systems since they have only one-third the number of remote valves as standard active safety systems and do not incorporate pumps.

The design would also not require HVAC, cooling water, and the associated seismic buildings to house these components. Emergency diesel generators would also require a network of support systems, air start, fuel storage tanks and transfer pumps, and the air intake/exhaust system. The primary safety systems include the emergency core cooling system, safety injection and depressurization, passive residual heat removal, and passive containment cooling system [33]. The passive core cooling system (PXS) protects the plant against leaks and ruptures of different sizes and locations. It provides core residual heat removal, safety injection, and depressurization. Three sources of water maintain core cooling through safety injection. Long-term injection water is supplied by gravity once the system is depressurized using a four-stage automatic depressurization system. A passive residual heat removal heat exchanger protects the plant from transients that upset the normal steam generator feed water and steam systems. The passive containment cooling system (PCS) provides the safety-related ultimate heat sink for the plant [33]. The steel containment vessel provides the heat transfer surface that removes heat from the containment vessel and transfers it to the atmosphere following an accident. The natural circulation of air does this, but after an accident, a heat-sensitive valve automatically opens, and water flows down to the reactor to remove the decay heat.

A containment vessel is a vital safety component of this reactor, like many other designs worldwide. The containment vessel is designed to contain the release of radioactive material following a nuclear accident, along with protecting the reactor pressure vessel from external hazards. It acts as a heat sink connection between the reactor and the in-containment refueling water storage tank [34]. The containment vessel is usually submerged in the reactor pool or is placed in a location that can be easily flooded by water stored in adjoining storage pools. During a loss-of-coolant accident (LOCA), the surrounding water would provide a passive heat sink for

the containment vessel to remove heat. The surrounding water or in-containment refueling water is also used to flood the reactor cavity for external cooling of the reactor pressure vessel during a severe accident. This type of reactor design safety system would work passively and thus would not depend on active components and safety grade support systems which are expensive and not guaranteed to function correctly during an emergency.

Generation IV nuclear reactor designs are meant to be highly economical, possess an enhanced safety system, and produce minimal waste. A number of these include Gas-cooled Fast Reactor (GFR), Lead-cooled Fast Reactor (LFR), Molten Salt Reactor (MSR), Supercritical Water-cooled Reactor (SCWR), Sodium-cooled Fast Reactor (SFR), and Very High-Temperature Reactor (VHTR) [35]. Generation IV reactors incorporate numerous passive safety elements. One of these includes replacing the water coolant with sodium [35]. The boiling point of sodium is around 300 to 400°C compared to water which has a boiling temperature of 100°C. As the temperature in the reactor increases, the liquid water coolant can begin to boil and convert to steam. Under these conditions, the water does not get a chance to condense back into liquid water, resulting in high-pressure steam bubbles. This decreases the amount of available coolant to control the decay heat. Sodium, on the contrary, would absorb heat to extreme temperatures without worrying about boiling away [35]. Sodium thus doesn't need to be circulating in a closed loop and can be applied as a pool. This pool design would not require external power as the coolant's circulation is unnecessary. Other Generation IV reactors use lead, helium, or supercritical water to cool the reactor core.

Furthermore, these reactors use uranium metal alloys that naturally prevent a runaway reaction during increasing core temperatures [35]. This uranium alloy expands naturally if

temperatures within the core begin to rise. The expansion of the alloy slows the runaway reaction by creating distance between two fissile nuclei which would decrease the chance of neutrons penetrating the nuclei. The main goal of the new Generation IV reactors is the safety of people and the environment.

3 CHAPTER: Melt Flow Solidification

Although various safety measures have been put into place to prevent severe nuclear power plant accidents, the possibility of equipment failure or natural disasters is still likely. A severe accident can lead to a reactor core meltdown within the nuclear power plant [2]. The molten material called corium, which results from a core meltdown, can begin to accumulate in the bottom of the calandria. The molten material can also enter moderator drain lines, moderator circulation lines, cooling pipes, and other devices [2]. A numerical model was created to simulate molten metal entering an initially empty vertical pipe, in which it would solidify and plug the pipe. An experimental setup was developed to validate the numerical model. This experimental setup used a low melting temperature metal, gallium, as a substitute for corium. The solidification and plugging of gallium in a vertical pipe were investigated. The experimental results were compared to an analytical model and numerical model of an equivalent event.

3.1 Numerical Model

A numerical model was developed in MATLAB to predict the penetration length of gallium in the vertical experimental setup. The numerical model was based on work done by Somers-Neal et al., which predicated the penetration length for a horizontal pipe flow [4], [36], [37]. One dimensional and transient governing equations were discretized by using the finite difference

method. The resulting equations were solved for the velocity of the molten metal, the temperature of the gallium, the temperature of the wall, and the amount of solidification occurring at each time-step. Due to the relatively small diameters of the test sections, a 1-D model was deemed appropriate for the numerical studies, but 2-D and 3-D numerical approaches should be studied in the future, when larger diameters will be considered. Numerous changes had to be made to the previous numerical model for it to be valid for a vertical orientation.

The most significant improvement to the numerical model was the consideration of potential energy change as gallium travels through the vertical pipe. This change has impacted all the fundamental equations of the numerical model. The energy conservation equation was written depending on the state of the control volume (CV): either full at the beginning of the time step or empty at the beginning of the time step but filled after the time step was complete. The CVs that were full at the start of the time-step were denoted as filled CVs, and those that were not filled at the beginning were represented as unfilled CVs. The bulk temperature equation of the CV was derived from the energy equation. For the unfilled CV, it was considered that there was no mass flow exiting, and the kinetic energy was negligible. This simplified the energy equation as shown in Eq. (3).

$$\frac{dU_{cv}}{dt} = \dot{Q}_{cv} + \dot{m}(h_i + g\Delta x) \quad (3)$$

where U_{cv} was the internal energy of the control volume (J), \dot{Q}_{cv} was the heat transfer rate (J/s), \dot{m} was the mass flow rate (kg/s), h_i was the enthalpy (J/kg), g was the gravitational acceleration (m/s^2), and Δx was the penetration node length (m). The simplified energy equation was then

integrated with respect to time and space, as seen in Eq. (4), and then rearranged to get a final equation for the bulk temperature of the unfilled CV, as shown in Eq. (5).

$$\int_0^{\Delta x} \int_0^{\Delta t} \frac{dU_{cv}}{dt} dxdt = \int_0^{\Delta x} \int_0^{\Delta t} -[h\pi D\Delta x(T_b - T_s)] dxdt + \int_0^{\Delta x} \int_0^{\Delta t} (h_i + g\Delta x) \frac{dm_{cv}}{dt} dxdt \quad (4)$$

$$T_b^{t+\Delta t} = -\frac{\left[h\pi D\Delta x \left(\left[\frac{T_{bi}^{t+\Delta t} + T_{bi}^t}{2} \right] - T_{wall}^t \right) \right] \Delta t}{2m_{cv}c_p} + \left[\frac{T_{bi}^{t+\Delta t} + T_{bi}^t}{2} \right] + \frac{g\Delta x}{2c_p} \quad (5)$$

where T_b was the bulk temperature of the gallium (K), T_{bi} was the inlet bulk temperature (K), D was the pipe diameter (m), T_{wall} was the wall temperature (K), m_{cv} was the mass in the CV (kg), Δx was the vertical node length (m), g was the gravitational constant (m/s^2), h was the convective heat transfer coefficient ($W/m^2 \cdot K$), c_p was the specific heat of gallium ($J/kg \cdot K$), Δt was the time difference (s), superscript t represented the current time-step, and superscript $t + \Delta t$ represented the next time-step. Similar to the unfilled energy equation, the simplified energy equation for the filled CV can be written as shown in Eq. (6).

$$\frac{dU_{cv}}{dt} = -h\pi D\Delta x(T_b - T_{wall}) + \dot{m}(\Delta h + g\Delta x) \quad (6)$$

Furthermore, the equation for the bulk temperature of the filled CVs was derived and rearranged, as shown in Eq. (7).

$$T_b^{t+\Delta t} = \frac{-\frac{h\pi D\Delta x\Delta t}{m_{cv}c_p} \left(\left[\frac{T_b^t}{2} \right] - T_{wall}^t \right) + \left(T_{bi}^{t+\Delta t} + \frac{T_{bi}^t}{2} - \frac{T_{be}^t}{2} \right) + \frac{g}{c}(\Delta x) + T_b^t}{\left(2 + \frac{h\pi D\Delta x\Delta t}{2m_{cv}c_p} \right)} \quad (7)$$

where T_{be} was the exit bulk temperature (K), i and e represented the inlet and exit conditions. Solidification of gallium would begin once the bulk temperature was determined to have reached the freezing temperature.

The velocity of the unfilled CV was derived by using the steady-state momentum equation. The height of gallium within the reservoir was assumed to be constant and was the primary driving force that caused the gallium to flow through the pipe. This is illustrated by z_{fixed} in Figure 11.

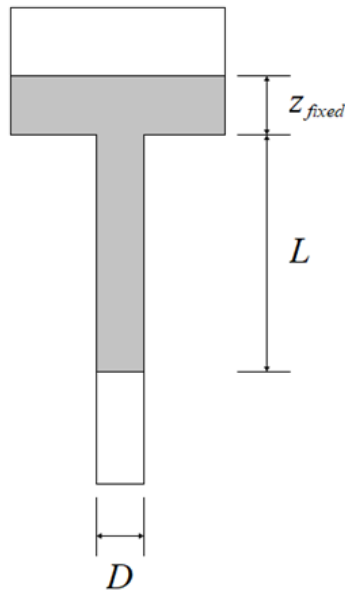


Figure 11: Sketch of the vertical pipe flow.

A notable consequence of the previously stated assumptions was a constant difference in pressure throughout the simulation. The velocity was calculated by considering losses due to contraction when the material freezes, known as entry and frictional losses. Entry losses used a streamline from the top of the reservoir to the front of the CV. The simplified momentum equation can be seen in Eq. (8), and the final velocity equation can be seen in Eq. (9).

$$m_{cv} \frac{dV_{cv}}{dt} = P_1 A_1 - P_2 A_2 - \tau_w \pi D L - \sum \frac{1}{2} K (\dot{m} V) + m_{cv} g \quad (8)$$

$$\frac{V_{cv}^{t+\Delta t} - V_{cv}^t}{\Delta t} = \frac{g}{L} \left[z_{fixed} - f \frac{L}{D} \frac{(V_{cv}^t)^2}{2g} - \sum K \frac{(V_{cv}^t)^2}{2g} + L \right] \quad (9)$$

where P was the pressure (Pa), A was the cross-sectional area of the pipe (m^2), τ_w was the shear stress (N), L was the length of pipe that the molten metal traveled (m), K was the loss coefficient, and f was the friction factor. The friction factor was determined assuming turbulent and incompressible flow and using the Churchill friction factor equations [38].

Because gravity now significantly impacts the flow, the acceleration will increase as the material flows through the pipe. The previous model used a constant time-step and grid spacing. This cannot be possible for a vertical configuration because the acceleration due to gravity would cause the molten metal to travel more than one node length in a single time step. Because the velocity was now changing in a different way than it was for the previous model, an adaptive time-step was introduced to ensure that the unfilled CVs were completely filled after each time step. The total time required to fill the CV could only be determined once the node length and leading node velocity were obtained. This time would then be used in consecutive time steps; therefore, the time step would progressively decrease to accommodate the acceleration of the flowing material.

The gallium properties were either modeled as constant values or using property relations. The dynamic viscosity, μ , thermal conductivity, k , and density, ρ , were determined using

equations that were a function of temperature and can be seen in Eq. (10), Eq. (11), and Eq. (12), respectively.

$$\mu = 0.4359e^{\frac{481}{T}} \quad (10)$$

$$k = 0.11T - 5 \quad (11)$$

$$\rho = 6.32723 - 7.3743 \cdot 10^{-4}T + 1.37767 \cdot 10^{-7}T \quad (12)$$

3.2 Experimental Setup

As previously stated, gallium was used as a corium substitute for the experimental setup. Corium is unavailable to the public since it is a mixture of melted nuclear reactor core material. It also has a high melting point, making testing difficult, dangerous, and expensive. A selection process was conducted to determine a substitute for corium. As a result, gallium was chosen because of its safety, availability, and low melting point relative to corium and other materials. In addition, gallium properties are well known. Indium and tin were also considered and could be used in future studies.

A sketch and photograph of the experimental setup can be found in Figure 12. The experimental setup was constructed based on a previously completed horizontal setup [4]. Modifications were done to the original design to account for the new vertical orientation of the experimental setup. The setup was designed to produce an apparatus that could predict the penetration length of gallium over multiple tests under the same conditions. The use of water and gallium drainpipes, solenoid valve to control gallium flow, easily changeable acrylic piping, and

a constant head tank system were used to make the testing easy to perform and to ensure the repeatability of the results.

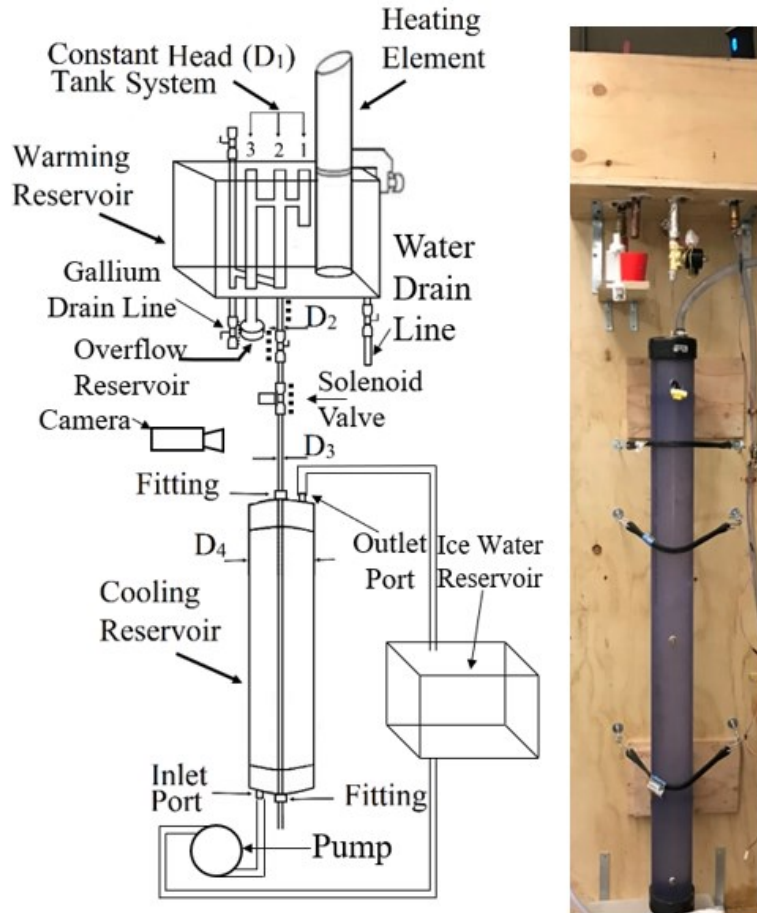


Figure 12: Sketch and photograph of the experimental setup.

The warming reservoir was placed on top of the experimental setup. The test procedure required that the warming reservoir be filled with water and then heated to a selected temperature above gallium's melting point. A specific heating element was used to heat the water to the required temperature and circulate the water evenly throughout the reservoir. The gallium was stored in containers which were placed into the warming reservoir to melt before the start of testing. The warming reservoir also ensured that the gallium would remain at the same temperature once it was

poured into the system. Heaters were used for the pipes outside the warming reservoir to maintain gallium at a nearly constant temperature (shown by dashed lines in Figure 12).

As shown in Figure 12, a constant head tank system was used to ensure that the gallium's height was maintained at the desired level through each consecutive test. This was done by using three different pipes. Pipe one was used for pouring gallium into the experimental apparatus, pipe two was used as a visual guide for monitoring the gallium level, and pipe three was connected to an overflow that allowed any excess gallium to be captured and used in future tests. This design made it feasible to get a constant height throughout the test. A solenoid valve was used to have a repeatable opening of the valve since having a manual valve made the experimental test less consistent due to the unpredictable manual process of opening the valve halfway. Copper piping was used for the constant head tank system but was then replaced by an acrylic tube after the solenoid valve. An acrylic tube was selected because it was made of a transparent material and thus would allow a slow-motion camera to capture and determine the gallium velocity. The camera was positioned to capture the velocity of the gallium before it entered the cooling reservoir. Precisely measured markings were made on the acrylic tube before it entered the cooling reservoir to know the exact distance so that the velocity of gallium could be determined using the camera. Once the distance that gallium travelled and the time in which it took the gallium to reach that distance was known, the initial velocity was calculated.

The acrylic tube passed through the cooling reservoir filled with ice water. Because of the height of the cooling reservoir, a temperature difference was possible between the top of the cooling reservoir and the bottom. To avoid this potential temperature difference, a pump was connected to an ice water reservoir which circulated the water through the inlet and then to the exit

of the cooling reservoir and back to the ice water reservoir. The ice water reservoir was consistently filled with ice to maintain the temperature. This allowed the water in the cooling reservoir to be held at a constant temperature throughout each test.

Once the test was complete, the gallium and water drain lines were used to remove water and gallium from the experimental apparatus. The water needed to be removed to prevent leaks, and the gallium was removed because when gallium freezes, it expands, which can cause damage to the experimental apparatus. Therefore, proper personal safety equipment was used during the testing process. The surrounding environment also had to be clear of any aluminium, since liquid gallium can corrode aluminium.

3.2.1 Measurement Uncertainty

Since there are no theoretical equations to determine the penetration length of gallium in a vertical pipe, an uncertainty analysis was performed. Several essential variables were determined to have the most significant impact on the penetration length. The variables include the temperature difference between the warming reservoir and the cooling reservoir (ΔT), the velocity of the gallium (V), and the diameter of the acrylic pipe (D). The uncertainty of the penetration length could then be determined with the following equations.

$$U_{X_P} = \pm \left[(B_{X_P})^2 + (t_v S_{X_P})^2 \right]^{\frac{1}{2}} \quad (13)$$

$$\frac{B_{X_P}}{X_P} = \left[\left(\frac{B_V}{V} \right)^2 + \left(\frac{B_D}{D} \right)^2 + \left(\frac{B_{\Delta T}}{\Delta T} \right)^2 \right]^{\frac{1}{2}} \quad (14)$$

where U_{X_p} represents the uncertainty, X_p represents the penetration length, t_v is a value from the Student's t-distribution table, S_{X_p} represents the random error in the penetration length, B represents the bias error, and the subscripts denote the bias error for each variable. The velocity of the gallium was calculated in a way that made it difficult to estimate the bias error directly. Therefore, the following equation was used to determine the bias error for the velocity variable.

$$B_V = \pm \left[\left(\frac{\partial V}{\partial t} B_t \right)^2 + \left(\frac{\partial V}{\partial d} B_d \right)^2 \right]^{\frac{1}{2}} \quad (15)$$

$$\frac{\partial V}{\partial d} = \frac{1}{t} \quad (16)$$

$$\frac{\partial V}{\partial t} = \frac{-d}{t^2} \quad (17)$$

where d represents the distance that the gallium is traveling (m) and t represents the period of the time (s). Utilizing these equations, the bias error for velocity can be determined. The distance gallium traveled when calculating the velocity was fixed at 10 cm and took an average time of 0.13 s. The slow-motion camera recorded the velocity at 240 frames per second. The bias error for the time was about 0.002 s, equivalent to half a frame. Furthermore, the bias error for the distance measurement was determined to be about 0.0005 m from the measurement tool used. With the information, the velocity bias error was determined to be 0.78 m/s. The acrylic pipe diameter was measured five different times, and the average was taken to calculate the final diameter. The average diameter was determined to be about 0.0034 m with a bias error of about 1.0×10^{-5} m. The bias error for the temperature difference was determined to be about 0.006 K, with an average temperature difference of about 40 K between the warming reservoir and the cooling reservoir. In

total, 12 tests were performed and used to calculate the value of the Student’s t-distribution. This value was determined to be 2.1 for a 95% confidence interval, and the random error for the experimental penetration length was about 0.04 m. Lastly, it was determined that the uncertainty for the penetration length was 0.08 m which resulted in about +/- 8% uncertainty with a 95% confidence interval.

3.3 Results and Discussion

An analytical model created by Best et al. was compared to the gallium numerical model and experimental results [8]. Twelve experimental tests were successfully completed. The velocities, Reynolds numbers, and corresponding penetration lengths are shown in Table 1.

Table 1: Experimental results for gallium, where V is the velocity, Re is the Reynolds number, and X_p is the penetration length.

Test #	V (m/s)	Re	X_p (m)
1	0.71	6650	1.11
2	0.72	6685	1.25
3	0.73	6836	1.39
4	0.79	7375	0.99
5	0.85	7919	1.20
6	0.83	7707	1.47
7	0.81	7503	1.16
8	0.76	7062	1.39
9	0.74	6860	1.14
10	0.77	7184	1.33
11	0.75	6950	1.05
12	0.82	7594	1.29

For the numerical model, a grid sensitivity study was conducted by calculating the penetration length at different control volume (CV) sizes. The outcome of this study showed that after about 1,570 CVs of 1 mm in length, the penetration length experienced very little change from an increasing number of CVs. Therefore, for the numerical model, a 1-mm CV size was used

to calculate the gallium penetration length. The comparison of the analytical model, numerical model, and experimental results can be seen in Figure 13.

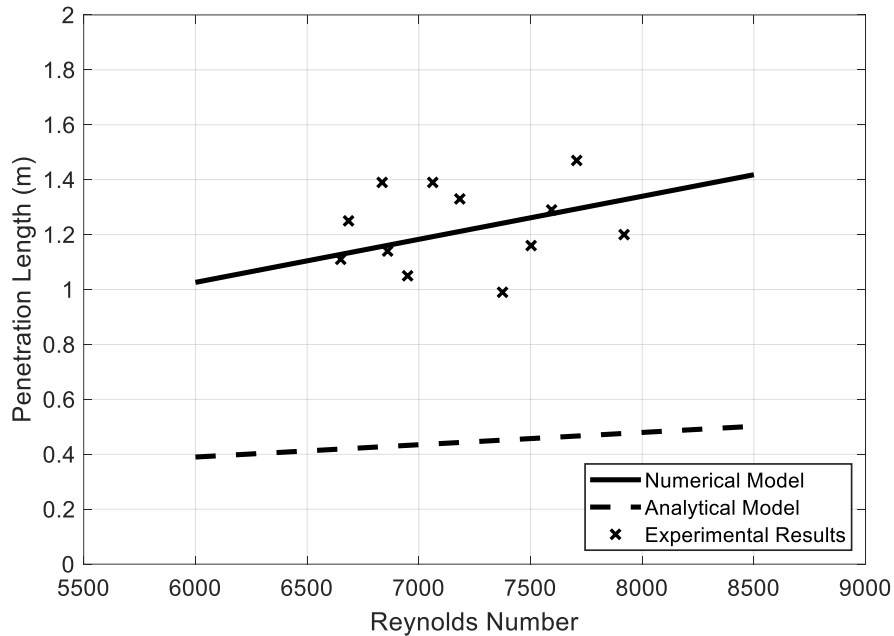


Figure 13: Comparison of the numerical, analytical, and experimental results for penetration length vs. Reynolds number.

The analytical model based on the work done by Best et al. was found to underpredict the penetration length significantly compared to the numerical model and experimental results [8]. The analytical model used multiple fundamental equations and simplifying assumptions to develop a closed-form equation that can be used to predict the penetration length. The discrepancies between these results can be attributed to several factors. The velocity and temperatures were updated throughout the numerical simulation, whereas the analytical model assumed constant velocity and temperatures [8]. Furthermore, the analytical model took gravity to be negligible, whereas the numerical simulation included the effects of gravity. Additionally, the analytical model assumed a constant friction factor determined using the Blasius friction factor equation for

turbulent flow. In contrast, the numerical model used Churchill's friction factor equations for turbulent flow conditions [38].

The numerical model results were found to have a percent error range from 1.4% to 20.4%, with the average being 10.3% compared to the experimental results. An explanation of these errors can be that the heat transfer coefficient used in the numerical model was derived using a previously published correlation. This correlation was used by Somers-Neal et al. in previous work, and it was concluded that it had several inherent errors associated with it [36]. The numerical model also had a degree of uncertainty in the gallium properties like thermal conductivity, density, and viscosity. Another significant error was observed when gallium filled the pipe. A pressure wave would travel back and forth through the liquid metal gallium [39]. The impact of this phenomenon was not accounted for in the numerical model and could have impacted the results of the experimental testing.

Several studies were done to investigate the numerical model results further. The leading node velocity of gallium was plotted as a function of the penetration length for three different Reynolds numbers. This can be seen in Figure 14, where a constant pipe diameter of 0.0034 m was used with varying starting velocities and final penetration lengths.

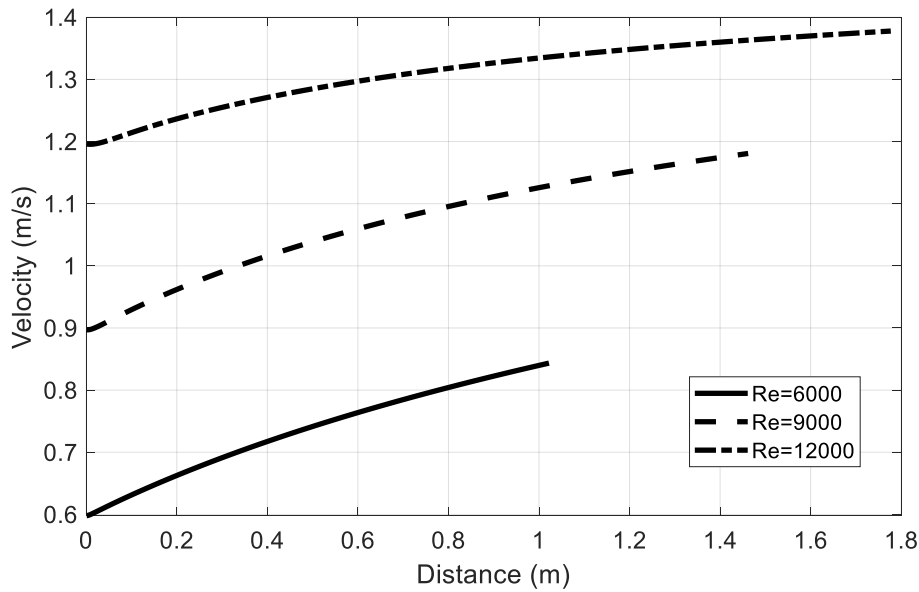


Figure 14: Comparison of leading node velocity vs. penetration length of gallium at different Reynolds numbers.

This study determined that the leading node velocity accelerated as the gallium filled the vertical pipe. For example, the velocity for a Reynolds number equal to 6,000 was half in value compared to the velocity of the 12,000 Reynolds number flow. The rate at which the velocity increased also followed a similar trend. This would suggest that the velocity of the liquid gallium does not need to reach a specific velocity value before it begins to freeze. The mass flow rate was continuously updated within the numerical model. This is required because as gallium travels down the pipe, it also solidifies on the pipe walls and creates a channel where the cross-sectional area decreases as the gallium solidifies. The reduction in the cross-sectional area was considered along with frictional losses in Eq. (9) in the summation of loss coefficients (K). The presence of losses should theoretically decrease the velocity, but because the total weight of gallium in the vertical pipe increases, this would cause an increasing force on the gallium, thus increasing the velocity.

Concerning the penetration length of gallium in the pipe compared to the Reynolds number, the penetration length increases with increasing Reynolds number. Likewise, the penetration length increases as the pipe diameter increases. This can be seen in Figure 15.

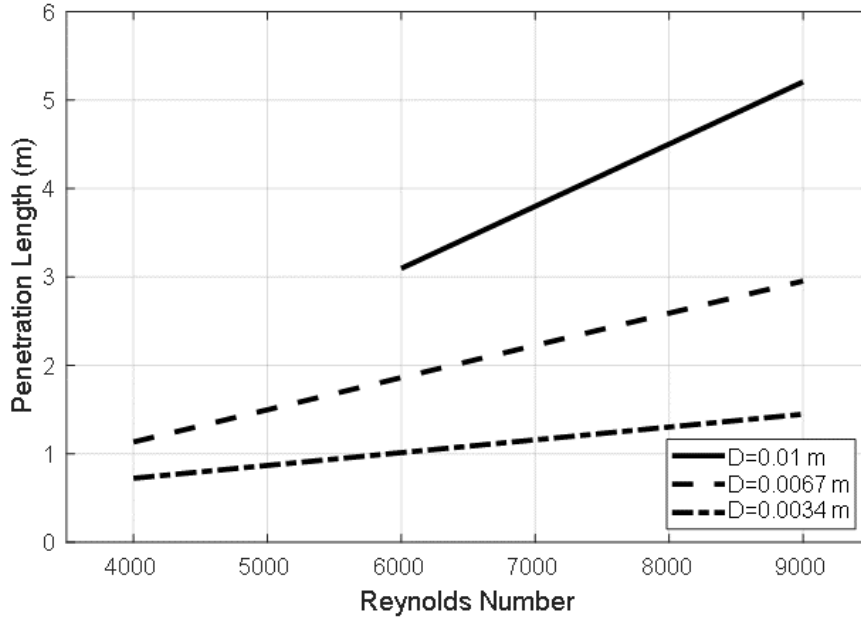


Figure 15: Comparison of penetration length of gallium vs. Reynolds number at different pipe diameters.

A simple equation can be derived to represent the penetration length of a 0.0034-m diameter pipe with respect to the Reynolds number.

$$x_p = 0.00017Re \tag{18}$$

Similar equations can be derived for other pipe diameters as the relationship between penetration length and Reynolds number is linear.

Using gallium as a substitute for corium in the experimental testing was not ideal. As mentioned, gallium was selected because of its low melting point, availability, and safety relative to corium and other materials. The primary purpose of using gallium in the experiments

was to validate the numerical results against real-world data. The same model was then used to estimate the penetration length for corium in a nuclear accident scenario. It is crucial to keep in mind the differences in thermofluidic properties between gallium and corium. For example, corium is a non-Newtonian fluid, and the numerical model would need to be updated to account for this fact. In addition, the detailed chemical and thermofluidic properties of the corium are not readily available. Considering that the proposed numerical model predominantly showed a greater agreement than the previous analytical model with the experimental results, it is expected the numerical model can be used to investigate corium solidification with reasonable accuracy. Therefore, this numerical model can be used to improve future designs of nuclear reactors to account for molten metal penetration and solidification in piping systems. To understand the corium behavior under different scenarios, the corium penetration length was compared to the Reynolds number at different pipe diameters. The results can be seen in Figure 16. Similar to the gallium results, as the Reynolds number and the pipe diameter increased, the penetration length also increased.

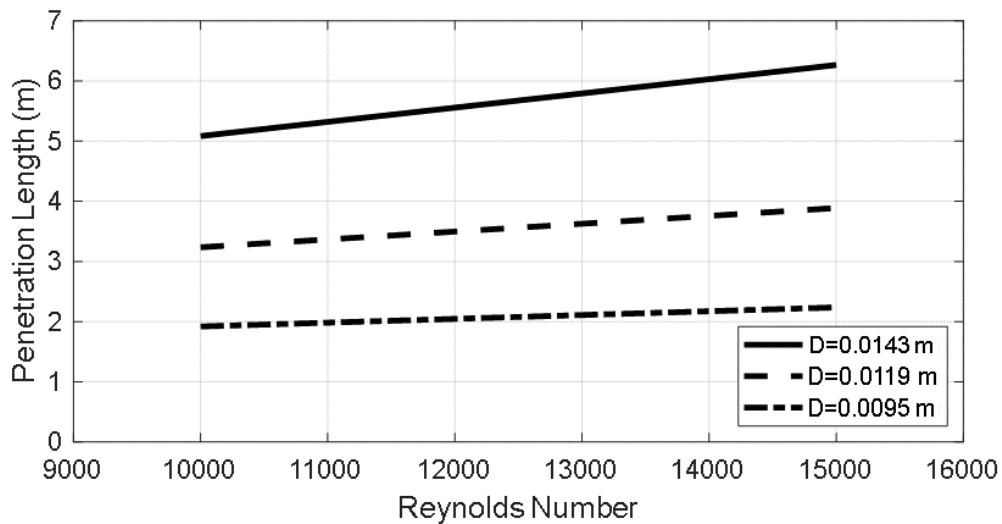


Figure 16: Comparison of penetration length of corium vs. Reynolds number at different pipe diameters.

At the exact moment of corium freezing, the radius of liquid corium was also investigated. The liquid radius size (mm) with respect to the penetration distance at three different Reynolds values can be seen in Figure 17. A complete blockage of the pipe occurs when the radius of the liquid corium reaches zero. As shown in Figure 17, the radius of the liquid corium is not equal to equal the radius of the pipe since a thin solid layer of corium is present. The thin solid layer thickness is imposed at the beginning of the simulation to be 0.25 mm. The liquid corium radius gradually decreases until complete blockage of the pipe occurs. The liquid corium traveling ahead of the blockage point would continue to penetrate the pipe until it reaches its final penetration length.

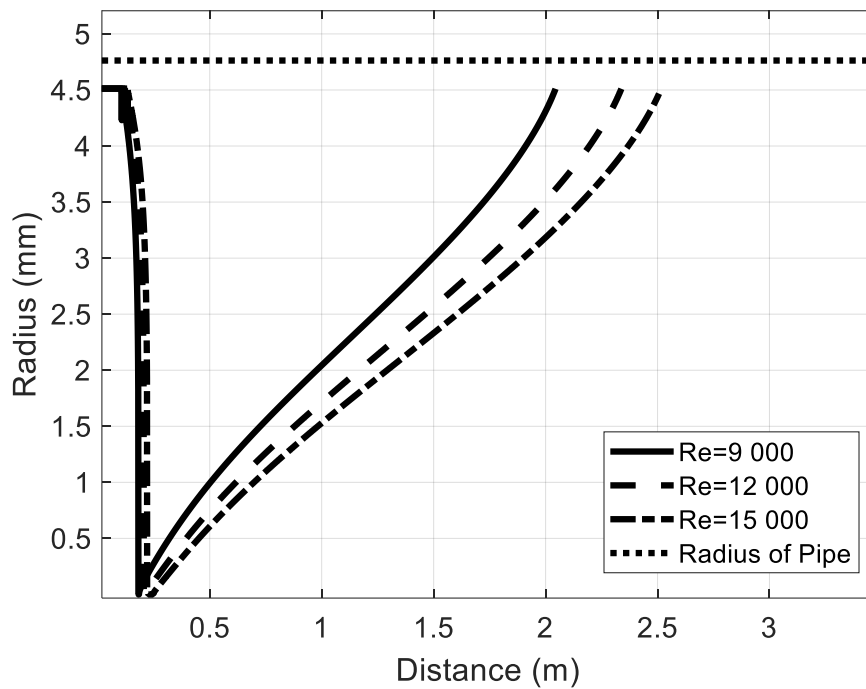


Figure 17: Radius of liquid corium vs. the penetration distance in the pipe for three different Reynolds numbers.

4 CHAPTER: Operational Limits of Liquid Metal Heat Pipes

The operating limits of a heat pipe must be considered during the design process as they inflict specific constraints on the choice of working fluid and wick structure used in the heat pipe. For instance, the sonic and viscous limits predominantly occur at low-temperature operating conditions and could impact the heat pipe's heat transfer abilities. On the contrary, the entrainment, capillary, and boiling limits may arise under high-temperature operating conditions.

In this chapter, the operational limits of heat pipes are studied for liquid metal heat pipes with different wick structures. The explanation of the numerical heat pipe model is in the proceeding sections.

4.1 Mathematical Model

A numerical model was created to determine the operating limits of a liquid metal heat pipe. This section highlights the mathematical theory used in determining each operating limit. The equations are referenced in the solution procedure section, explaining the model details.

4.1.1 Heat Pipe Properties

The heat pipe working fluid and wick structure are the two main physical properties that impact the heat pipe operating limits. The equations needed to calculate various heat pipe properties are explained in this section. These properties are listed below.

- Working fluid type.
- Pipe wall material and dimensions, including the outer diameter (D_{out}), thickness (t_{wall}), evaporator length (L_e), adiabatic length (L_a) and condenser length (L_c).

- Existence of a wick: thermosiphon vs. heat pipe.
- Wick type, material, and structural characteristics.

Liquid metal potassium was selected as the working fluid for this numerical model. The fluid thermodynamic properties can then be calculated from temperature correlations. Other main dimension parameters are the inner radius of the pipe wall (r_{in}), total length (L_{tota}), the total effective length ($L_{eff,t}$), the total powered effective length ($L_{eff,s}$) which can be calculated from Eqs. (19) to (22). The total effective and powered effective lengths are derived by assuming the power is uniformly applied to the evaporator and removed from the condenser. The material of the wall and wick determine the thermal conductivity (k) value.

$$r_{in} = \frac{D_{out} - t_{wall}}{2} \quad (19)$$

$$L_{tota} = L_e + L_a + L_c \quad (20)$$

$$L_{eff,t} = \frac{L_e}{2} + L_a + \frac{L_c}{2} \quad (21)$$

$$L_{eff,s} = \frac{L_e}{2} + \frac{L_c}{2} \quad (22)$$

The main focus of the numerical model is on heat pipes containing a wick. A screen mesh, annual-gap mesh, and arterial mesh are the different wick structures considered in the numerical model and are shown in Figure 18. Annular-gap mesh and arterial mesh are commonly implemented for liquid metal heat pipes [40].

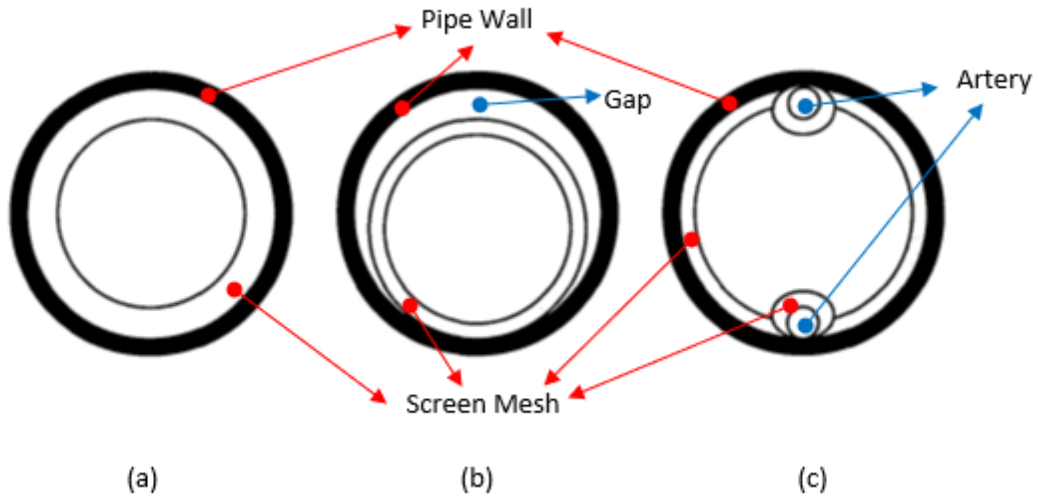


Figure 18: Wick structure schematic: (a) screen mesh, (b) annular-gap mesh, and (c) arterial mesh [40].

4.1.1.1 Screen Mesh

A screen mesh wick structure is made by wrapping several layers of metal mesh screen into a cylindrical shape and then placing it into the pipe. The following parameters are necessary to model the screen mesh.

- Mesh number ($N_{mesh,in}$) is the number of the wires spaced evenly in the one-inch length of the mesh.
- Layer number (N_{layr}) is the number of screen layers.
- Wire diameter (D_{wire}) is the diameter of the wire in the screen.
- Layer compressibility (β_{layr}) is how the layers can be compressed against each other compared to being apart by one diameter of the wire.

The mesh number (N_{mesh}) can be represented in SI unit ($1/m$) using Eq. (23). The layer compressibility (β_{layr}) can be any value larger than zero. When the layer compressibility value is

equal to one, the gap between the two layers of a screen mesh is equal to the diameter of the screen wire. A compressibility value greater than one means that the layers have a distance lower than the wire diameter. The layer compressibility is used in Eq. (24) to (26) to determine the wick thickness (t_{wick}), the vapor channel radius (r_v), and area (A_v). The cross-sectional area of the liquid flow (A_l) is then obtained from Eq. (27).

$$N_{mesh} = \frac{N_{mesh,in}}{0.0254} \quad (23)$$

$$t_{wick} = \frac{2N_{layer}D_{wire}}{\beta_{layer}} \quad (24)$$

$$r_v = r_{in} - t_{wick} \quad (25)$$

$$A_v = \pi r_v^2 \quad (26)$$

$$A_l = \pi(r_{in}^2 - r_v^2) \quad (27)$$

Additionally, the mesh effective pore radius (r_{eff}), porosity (φ), and permeability (κ) of the mesh wick are obtained from Eqs. (28) to (30) as described in Table 3.1 of Ref. [41]. Then, the effective thermal conductivity of the wick (K_{eff}) is also obtained from Eq. (31) from the thermal conductivity of wick and liquid flow [41].

$$r_{eff} = \frac{1}{2N_{mesh}} \quad (28)$$

$$\varphi = 1 - \frac{1.05\pi N_{mesh}D_{wire}}{4} \quad (29)$$

$$\kappa = \frac{D_{wire}^2 \varphi^3}{122(1 - \varphi)^2} \quad (30)$$

$$K_{eff} = K_l \frac{(K_l + K_{wick}) - (1 - \varphi)(K_l - K_{wick})}{(K_l + K_{wick}) + (1 - \varphi)(K_l - K_{wick})} \quad (31)$$

4.1.1.2 Annular-gap Mesh

An annular-gap mesh wick consists of a gap between the pipe wall and the screen mesh, as shown in Figure 18. The thickness of the gap can be either even in all radial directions or not. The average (t_{gap}) is an important input parameter needed to obtain the dimension parameters of an annular-gap mesh wick structure. The wick thickness is calculated from Eq. (32), and the radius and area of the vapor channel can be calculated from Eq. (25) and (26), respectively. The liquid channel area, A_l , is calculated using Eq. (33) and assuming that the liquid flows axially in the gap.

$$t_{wick} = t_{gap} + t_{wick,mesh} \quad (32)$$

$$A_l = \pi(r_{in}^2 - (r_v + t_{wick,mesh})^2) \quad (33)$$

where $t_{wick,mesh}$ is calculated from Eq. (24). Having the gap improves the wick permeability while retaining the high capillary forces of the screen mesh. However, the gap may cause initial difficulties when priming the wick during the start-up [40]. For this wick design, the wick porosity is set to one, and the effective pore radius is required for the screen mesh part from Eq. (28). The permeability calculation, as presented in Eq. (34), is more elaborate than that of the screen mesh wick [41]. The permeability value obtained from this correlation is only valid for laminar liquid flow in the wick.

$$\kappa = \frac{D_{hyd}^2 \varphi}{2fRe_{l,hyd}} \quad (34)$$

$$where: \left\{ \begin{array}{l} D_{hyd} = 2(R_1 - R_2), \quad fRe_{l,hyd} = \frac{16(1 - R^*)^2}{1 + R^{*2} - 2R_m^{*2}} \\ R_m^* = \left(\frac{1 - R^{*2}}{2 \ln \left(\frac{1}{R^*} \right)} \right)^{0.5}, \quad R^* = \frac{R_2}{R_1} \\ R_1 = r_{in}, \quad R_2 = r_{in} - t_{gap} \end{array} \right.$$

The effective thermal conductivity has two components, one for the gap and another for the screen mesh section. The gap section is the liquid thermal conductivity, and the screen mesh section is calculated from Eq. (31). The total thermal conductivity of the wick is obtained from Eq. (35) [41].

$$K_{eff} = \frac{(t_{gap} + t_{wick,mesh})K_l K_{wick,mesh}}{t_{gap}K_l + t_{wick,mesh}K_{wick,mesh}} \quad (35)$$

4.1.1.3 Arterial Mesh

Lastly, the arterial mesh structure includes artery channels that allow the axial liquid to flow to the screen mesh, as illustrated in Figure 18. The artery wall is made of a screen mesh or perforated metal sheet. Modeling this wick structure requires two additional parameters, including the diameter (D_{arty}) and number of arteries (N_{arty}). The dimension parameters can be calculated from equations introduced in the screen-mesh wick section. The liquid flow area can be calculated from Eq. (36) as the liquid axial flow is assumed to only be through the arteries. Considering this assumption and considering the flow is laminar and the porosity is equal to one, the permeability can be obtained using Eq. (37) [41].

$$A_l = N_{arty} \pi \left(\frac{D_{arty}}{2} \right)^2 \quad (36)$$

$$\kappa = \frac{1}{8} \left(\frac{D_{arty}}{2} \right)^2 \quad (37)$$

The arterial mesh design, like the annular-gap mesh, retains the high capillary forces at the wick/vapor interface and results in a high wick permeability. A shortcoming of this wick design is the possibility of vapor bubbles forming inside the arteries during the start-up process. If the bubbles do not collapse, they may prevent the subcooled liquid from traveling from the condenser to the evaporator [40]. Lastly, the effective thermal conductivity is calculated from Eq. (31).

4.1.2 Vapor Flow

This section calculates the required properties in the vapor flow region using saturation correlations for potassium [42]. The density of the vapor can be determined from saturation correlations or the ideal gas relation. The vapor density is calculated from Eq. (38) using the ideal gas assumption when the given pressure and temperature values are known.

$$\rho = \frac{P}{RT} \quad (38)$$

where R is the specific gas constant, P is the pressure, and T is the temperature of the vapor. The mass flow rate is determined using Eq. (39), given that the power and latent heat are known.

$$\dot{m} = \frac{\dot{Q}}{h_{fg}} \quad (39)$$

where \dot{Q} is the power at the evaporator exit and h_{fg} is the latent heat of the evaporation. The mass flow rate can be used to obtain the velocity at the evaporator exit using Eq. (40).

$$u_{evap,exit} = \frac{\dot{m}}{\rho_v A_v} \quad (40)$$

As shown in Eq. (41) and Eq. (42), the sonic velocity can be determined for an isothermal or isentropic case.

$$a_{isothermal} = (RT)^{0.5} \quad (41)$$

$$a_{isentropic} = (\gamma RT)^{0.5} \quad (42)$$

where γ is the specific heat ratio of the vapor. The Mach number can be determined using the velocity and sonic velocity. This equation is shown below in Eq. (43).

$$M = \frac{u}{a} \quad (43)$$

4.1.2.1 Viscous Pressure Drop

The viscous pressure drop that is present due to friction in the evaporator and condenser can be obtained using Eq. (44).

$$\Delta P_{vap,vis} = \frac{cmafRe}{2r_v^2 A_v \rho_v} \mu_v \dot{m} L_{eff,s} \quad (44)$$

where cma is the compressibility factor, f is the Fanning friction factor, μ_v is the dynamic viscosity of vapor, and $L_{eff,s}$ is the effective length without the adiabatic section.

The compressibility factor, cma , can be determined using Eq. (45) [43]. The value of cma is determined by the flow state. If the flow is incompressible, then the value of cma would be unity. On the other hand, if the flow is compressible then the cma value is determined using the equation.

$$cma = \begin{cases} 1 & Ma < 0.2 \text{ Incompressible} \\ \left(1 + \frac{\gamma(M-1)}{2M^2}\right)^{-0.5} & Ma > 0.2 \text{ Compressible} \end{cases} \quad (45)$$

The Fanning factor can be calculated from the Churchill correlation presented in Eq. (46). The correlation is valid for laminar, transient, and turbulent flows [44].

$$f = 2 \left[\left(\frac{8}{Re} \right)^{12} + \left(\frac{1}{(A+B)^{\frac{3}{2}}} \right) \right]^{\frac{1}{12}} \quad (46)$$

$$\text{where: } A = \left\{ 2.457 \ln \left[\frac{1}{\left(\frac{7}{Re} \right)^{0.9} + 0.27 \frac{\varepsilon}{D_v}} \right] \right\}^{16}, \quad B = \left(\frac{37530}{Re} \right)^{16}$$

where ε represents the surface roughness of the pipe and Re is the Reynolds number defined by Eq. (47) for a fluid flow inside a pipe.

$$Re = \frac{\rho_v u D_v}{\mu_v} \quad (47)$$

The vapor diameter (D_v) is used as the characteristic length for a circular vapor channel. The vapor viscosity can be calculated from the saturation correlations.

4.1.2.2 Fanno Flow for Adiabatic Section

Fanno flow equations can be used to calculate specific property values of the vapor at the condenser inlet if an adiabatic section is present in the heat pipe. The Fanno flow method would require an iterative process to obtain results since it assumes that friction is present, the process is adiabatic, and the fluid is an ideal gas with constant specific heat. The Mach number is first calculated using the velocity of the flow. The Fanno flow factor (FF) is then obtained using Eq. (48) for a point in the adiabatic section, such as the evaporator exit [45]. The Fanno flow relation, Eq. (49), can be used to determine the Fanno flow factor and Mach number at any other location along the adiabatic section like the condenser inlet. It is important to note that the isentropic definition of sonic velocity should be used in the Fanno flow calculations.

$$FF = \frac{1 - M^2}{\gamma M^2} + \frac{\gamma + 1}{2\gamma} \ln \frac{(\gamma + 1)M^2}{2 + (\gamma + 1)M^2} \quad (48)$$

$$\frac{4fL_a}{D_v} = FF_{evap,exit} - FF_{cond,inlet} \quad (49)$$

The pressure ratio at a specific location to the choked pressure (Pr) can be determined from Eq. (50). Using this parameter, the pressure ratio between the evaporator exit and condenser inlet can be obtained as shown in Eq. (51).

$$Pr = \frac{1}{M} \left(\frac{\gamma + 1}{2 + (\gamma + 1)M^2} \right)^{0.5} \quad (50)$$

$$\frac{P_{evap,exit}}{P_{cond,inlet}} = \frac{Pr_{evap,exit}}{Pr_{cond,inlet}} \quad (51)$$

For instance, the pressure at the condenser inlet can be determined if the pressure at the evaporator exit is known. The temperature at the condenser inlet is determined using the saturated correlations. The sonic velocity is also determined from the temperature to obtain the vapor velocity. Knowing the two pressure values, the pressure drop in the adiabatic section can be calculated.

4.1.3 Liquid Flow

Similar to the vapor flow section, the viscous liquid pressure drop is calculated using Eq. (52). The gravitational or tilt pressure change in the liquid channel is obtained using Eq. (53). It is important to note that the gravity radial effect on the liquid pressure change is assumed to be negligible [46].

$$P_l = \frac{\mu_l \dot{m} L_{eff,t}}{\kappa A_l \rho_l} \quad (52)$$

$$\Delta P_g = \rho_l g L_{tota} \sin(\theta) \quad (53)$$

where κ is the wick permeability, g is the gravitational constant, θ is the tilt angle, L_{tota} is the total length, and $L_{eff,t}$ is the total effective length.

4.1.4 Viscous Limit

In heat pipes, the viscous limit occurs when the viscous forces in the vapor flow cause the pressure at the condenser to reach zero. Consequently, the vapor flow becomes very low or stops altogether. The viscous limit is determined using Eq. (54) [47].

$$\dot{Q}_{vis} = \frac{A_v D_v^2 h_{fg} \rho_0 P_0 (1 - G^2)}{64 \mu_v L_{eff,t}} \quad (54)$$

$$\text{where: } G = \frac{P_{cond,end}}{P_0} = 1 - \frac{\Delta P}{P_0}$$

where the subscript 0 represents the stagnation point at the evaporator end cap. The effective length ($L_{eff,t}$), is equivalent to the sum of the adiabatic length plus half of each condenser and evaporator length when the heat load is applied to and removed from the heat pipe with a uniform radial heat flux. Three different methods are considered where the evaporator exit pressure (P_o), experienced a pressure drop of 10%, 70%, or 100%. In Eq. (54), G represents the minimum to maximum vapor pressure ratio at the evaporator and condenser caps and is set to 0.1, 0.7, or 1.0 for the three different methods studied. These methods assume that the pressure drop is equal to the vapor pressure at the evaporator end. Furthermore, the vapor temperature at the evaporator is assumed to be isothermal, and the fluid is considered an ideal gas under laminar flow conditions.

An alternative method to determine the viscous limit takes an initial guess of the applied power and iterates on it until the pressure drop due to friction is equal to the fluid pressure at the evaporator exit. Similarly, another iterative method exists where iteration is done on the applied power, but the friction in the adiabatic section is determined using the Fanno flow equations [45]. For these two methods, the stagnation vapor pressure is assumed to be saturated pressure, and the conditions are isentropic when determining the speed of sound and using Fanno flow equations. The vapor flow section also explains these two iterative methods.

4.1.5 Sonic Limit

The sonic limit can occur when the vapor flow reaches the speed of sound at the evaporator exit or the condenser inlet. This can limit the amount of heat transferred through the heat pipe. The sonic limit can be expressed in a closed-form equation by considering a one-dimensional vapor flow. The applied heat is assumed to be uniform at the evaporator, and only the inertia effects are considered. The vapor is assumed to act as an ideal gas to determine the fluid properties. The sonic limit can be determined using Levy's equation, Eq. (55).

$$\dot{Q}_{son} = A_v \rho_0 h_{fg} \left(\frac{\gamma R T_0}{2(\gamma + 1)} \right)^{0.5} \quad (55)$$

where $\gamma R T_0$ can be replaced by a_0^2 as proposed by Faghri [41]. The stagnation temperature can be determined using Eq. (56) under isentropic conditions where T is the choked temperature. However, under isothermal conditions, the stagnation temperature would be equivalent to the evaporator exit temperature.

$$T_0 = T \left(1 + \frac{\gamma - 1}{2} \right) \quad (56)$$

A correction factor of 0.986 is applied to the velocity to account for the axial vapor velocity variation across the cross-sectional area. For this, Eq. (43) is multiplied by 0.986 when obtaining the velocity. For laminar and isothermal vapor flow, the sonic limit can be calculated at the evaporator exit using Eq. (57) [48].

$$\dot{Q}_{son} = 0.474 A_v h_{fg} (\rho_0 P_0)^{0.5} \quad (57)$$

It is important to note that this equation is not applicable for long heat pipes or low-temperature operating conditions because the isothermal assumption is not valid. An alternative iterative solution can be used to determine the applied power at which the vapor velocity would equal the sonic velocity at the condenser inlet. Considering that if an adiabatic section is present, the vapor velocity at the evaporator exit will be subsonic when the vapor flow reaches the sonic velocity at the condenser inlet.

The sonic limit can be obtained using Eq. (58), which Busse [47] proposed as an iterative solution given that viscous effects in the adiabatic section are considered.

$$\dot{Q}_{son} = A_v h_{fh} \left(\frac{1 - \frac{1}{Pr_0}}{APr_0} \rho_0 P_0 \right)^{0.5} \quad (58)$$

where A is a constant equal to 1.11 for this method. The stagnation pressure ratio Pr_0 is the pressure at the evaporator end over the pressure at the evaporator exit, as shown in Eq. (59). It is important to note that the vapor is assumed to be in a stagnation condition at the evaporator end.

$$Pr_0 = \frac{P_0}{P_{v,evap,exit}} \quad (59)$$

The stagnation pressure at the evaporator end is determined using Eq. (60). The viscous pressure drop and the inertial pressure drop are obtained using Eq. (61) and Eq. (62), respectively.

$$P_0 = \Delta P_i + \Delta P_{vis} + P_{v,evapexit} \quad (60)$$

$$\Delta P_{vis} = \frac{8\mu_v u_{evap,exit} L_e}{r_v^2} \frac{L_e}{2} \quad (61)$$

$$\Delta P_i = 1.11\rho_v u_{evap,exit}^2 \quad (62)$$

Another method similar to Busse's [47] iterative approach uses Eq. (57) to obtain the sonic limit assuming that there is viscous flow in the adiabatic section and that the stagnation pressure is obtained directly from the condenser inlet pressure. The pressure at the evaporator end used for the calculation is determined using Eq. (63).

$$P_0 = 2.08P_{cond,inlet} \quad (63)$$

$$\text{where: } P_{cond,inlet} = \frac{P_{evap,exit}}{Pr_{cond,inlet}}$$

A final iterative method is a modified version of Busse's [47] Eq. (58). In this method, the sonic limit is determined assuming that there is viscous flow in the adiabatic section and that the stagnation pressure is obtained from the evaporator exit pressure. The A and Pr_0 are determined by solving Eq. (64) to Eq. (67) simultaneously.

$$A \equiv \frac{\overline{u^2}}{\bar{u}^2} = 1.234 - 0.358g + -0.206g^2 \quad (64)$$

$$g = 2.14 \frac{x - 0.310 - (1.145x - 0.669)^{0.5}}{x - 0.765} \quad (65)$$

$$x = \frac{Pr_0 - 1}{\ln Pr_0} \quad (66)$$

$$Pr_0 - 1 = AM_{evap,exit}^2 \quad (67)$$

The equation used to determine Pr_0 Eq. (67) is derived from the inertial pressure drop equation proposed by Busse [47] using the ideal gas equation and assuming an isothermal sonic velocity in the evaporator section.

4.1.6 Capillary Limit

The capillary limit occurs when the capillary forces in the heat pipe wick cannot prevent the high-pressure vapor from penetrating the wick. A heat pipe reaches its capillary limit when the sum of all pressure drops is equal to the capillary forces. This would cause the evaporator to dry out and the heat pipe to fail. When examining the capillary limit, the evaporation and condensation pressure drops are often neglected [40]. An iterative process must be done to solve the capillary limit, where the capillary pressure and pressure drops are calculated and compared until their difference reaches zero. The capillary pressure is determined using Eq. (68) and assuming a contact angle of zero. The capillary limit, which occurs when the total pressures are equal to the capillary forces, can be obtained using Eq. (69).

$$\Delta P_{cap} = \left(\frac{2\sigma}{r_{eff}} \right) \quad (68)$$

$$\Delta P_{cap} = \Delta P_l + \Delta P_v + \Delta P_i + \Delta P_g \quad (69)$$

where σ is surface tension, r_{eff} is the wick effective pore radius, subscript l indicates liquid, v indicates vapor, i indicates the pressure changes due to vapor acceleration or deceleration, and g

indicates gravity. The capillary limitation varies based on the wick structure, working fluid, evaporator heat flux, and operating temperature.

The capillary limit can also be determined using a method proposed by Reay & Kew [46]. Before the capillary limit is determined, the mass flow rate is first obtained using Eq. (70), after which Eq. (71) can be used to obtain the capillary limit.

$$\dot{m} = \left[\frac{\rho_l \sigma}{\mu_l} \right] \left[\frac{\kappa A}{L_{total}} \right] \left[\frac{2}{r_c} - \frac{\rho_l g L_{total} \sin \theta}{\sigma} \right] \quad (70)$$

$$\dot{Q}_{cap} = \dot{m}_{max} h_{fg} = h_{fg} \left[\frac{\rho_l \sigma}{\mu_l} \right] \left[\frac{\kappa A}{L_{total}} \right] \left[\frac{2}{r_c} - \frac{\rho_l g L_{total} \sin \theta}{\sigma} \right] \quad (71)$$

In this method, the pressure drop in the evaporator is neglected, and all the fluid properties are determined at the evaporator exit temperature. The liquid properties are assumed to be constant along the heat pipe, which has a uniform wick and applied power.

An alternative method proposed by Chi [43] uses Eq. (72) to determine the capillary limit. For this equation, the liquid and vapor pressure drop factors are required [43]. They are obtained using Eq. (73) and Table 2, respectively.

$$\dot{Q}_{cap} = \frac{\Delta P_{cap} - \Delta P_g}{(F_l + F_v) L_{eff,t}} \quad (72)$$

$$F_l = \frac{\mu_l}{k A_l \rho_l h_{fg}} \quad (73)$$

Table 2: Vapor frictional term for different flow cases [43]

$Re_v (\rho_v \mathbf{u}_v D_v / \mu_v)$	$M_v (\mathbf{u}_v / \sqrt{\gamma R T_v})$	F_v
$Re_v \leq 2300$	$M_v \leq 0.2$	$\frac{8\mu_v}{A_v R_v^2 \rho_v h_{fg}}$
$Re_v \leq 2300$	$M_v > 0.2$	$\frac{8\mu_v}{A_v R_v^2 \rho_v h_{fg}} \left(1 + \frac{\gamma - 1}{2} M_v^2\right)^{-0.5}$
$Re_v > 2300$	$M_v \leq 0.2$	$\frac{0.019\mu_v}{A_v R_v^2 \rho_v h_{fg}} \left(\frac{2R_v \dot{Q}}{A_v \mu_v h_{fg}}\right)^{0.75}$
$Re_v > 2300$	$M_v > 0.2$	$\frac{0.019\mu_v}{A_v R_v^2 \rho_v h_{fg}} \left(\frac{2R_v \dot{Q}}{A_v \mu_v h_{fg}}\right)^{0.75} \left(1 + \frac{\gamma - 1}{2} M_v^2\right)^{-0.5}$

A modified simplified Chi [43] method assumes an incompressible laminar vapor flow regime and thus F_v is equal to the first-row value of Table 2. In both Chi methods, the liquid properties are assumed to be constant along the pipe, which also has a uniform wick and uniform power distribution at the evaporator and condenser.

A final iterative method can also be used to determine the capillary limit. This method requires the inertial evaporator pressure drop to be determined using Eq. (74), and the final vapor pressure drop in the evaporator would be obtained using Eq. (75) when $\Delta P_{vap,evap}$ on the right side of the equation is obtained from the vapor flow section equations, Eq. (44).

$$\Delta P_{i,evap} = \frac{1.33}{\rho_v} \left(\frac{\dot{m}}{A_v}\right)^2 \quad (74)$$

$$\Delta P_{vap,evap} = \Delta P_{i,evap} + \frac{\Delta P_{vap,vis} \left(\frac{L_e}{2}\right)}{L_{eff,s}} \quad (75)$$

Similarly, for the condenser inlet, the Mach number is found using Fanno flow equations, and a is the isentropic sonic velocity at the condenser inlet. The inertial pressure drop in the condenser, assuming total inertial pressure recovery, is determined using Eq. (76). Lastly, Eq. (77) is used to determine the vapor pressure drop in the condenser.

$$\Delta P_{i,cond} = 1.33\rho_v(Ma)_{cond,inlet}^2 \quad (76)$$

$$\Delta P_{vap,cond} = -\Delta P_{i,cond} + \frac{\Delta P_{vap,vis} \left(\frac{L_c}{2}\right)}{L_{eff,s}} \quad (77)$$

4.1.7 Entrainment and Flooding Limit

The entrainment limit in a heat pipe can occur when the vapor and liquid flow past each other. If the vapor is traveling at large vapor velocities past the liquid, vapor shear stress can remove liquid droplets from the inner wick surface and transport them back to the condenser. Since liquid at the evaporator is depleted, the evaporator can dry out, and the heat pipe may fail. Similar to the sonic limit, the entrainment limit can occur at the evaporator exit or the condenser inlet. Therefore, determining if an adiabatic section is present in the heat pipe is crucial. Entrainment in a heat pipe will occur when the Weber number, also known as the ratio of vapor dynamic pressure to liquid surface tension, is equal to or greater than one. This is shown below in Eq. (78) [46]. The entrainment limit value is determined using the equation shown in Eq. (79) [41].

$$We = \frac{\rho_v u^2 z}{2\pi\sigma} \geq 1 \quad (78)$$

$$\dot{Q}_{ent} = A_v h_{fg} \left(\frac{2\pi\sigma\rho_v}{z}\right)^{0.5} \quad (79)$$

where σ is surface tension, and the length (z) characterizes the liquid/vapor interface at the inner wick surface. The saturation fluid correlations can determine the vapor density and the liquid surface tension. According to Faghri [41], the z parameter can be set to equal twice the hydraulic perimeter of the pores on the inner wick surface. For wicks with a screen mesh inner surface, the z parameter can be calculated from Eq. (80). Sterbentz [49] and Reay & Kew [46] proposed different values of z for the wicks with a mesh inner surface as shown in Eq. (81) and (82), respectively. The former reference also recommended calculating the entrainment limit at the condenser inlet if the adiabatic section exists.

$$z = 4\pi\left(r_{eff} - \frac{D_{wire}}{2}\right) \quad (80)$$

$$z = \frac{D_{wire}}{2} \quad (81)$$

$$z = 2r_{eff} \quad (82)$$

Another equation, Eq. (83), was proposed by Prenger & Kemme [50] to determine the entrainment limit of heat pipes with a screen mesh. It is essential to mention that this equation is presented for gravity-assisted liquid metal heat pipes, which use knurled internal surface textures as a wick.

$$\dot{Q}_{ent} = \frac{A_v(2\pi)^{0.5}}{\delta_w^*} h_{fg}(\sigma\rho_v\delta_w)^{0.5} \quad (83)$$

where δ_w is the depth of the textured surface which has a reference depth (δ_w^*) of 7.4×10^{-4} m. For the wicks with a screen mesh inner surface, δ_w is equal to the screen wire radius, $\frac{D_{wire}}{2}$. The

entrainment limit is obtained using the critical Weber number and a vapor-dominated phenomenon at the evaporator exit while assuming a laminar flow condition.

An alternate method to determine the entrainment limit involves guessing the applied power and then iterating until the Weber number at the location of highest vapor velocity is equal to one. Similarly, another method iterates on the temperature at the condenser inlet while assuming the Weber number is equal to one. These two methods are also explained in the vapor flow section.

Iteration can also be used by calculating the limit at a specific evaporator exit temperature. If the tilt angle is 90 degrees and thus the pipe is in the vertical position, for a wickless pipe (thermosyphon), the entrainment limit can be calculated using Eq. (84) [46].

$$\dot{Q}_{ent} = c^2 A_v h_{fg} \frac{(g\sigma(\rho_l - \rho_v))^{0.25}}{(\rho_l^{-0.25} + \rho_v^{-0.25})^2} \quad (84)$$

$$\text{where: } a = 2r_{in} \left(\frac{g(\rho_l - \rho_v)}{\sigma} \right)^{0.5}, b = 0.5a^{0.25}, c = 3.2^{0.5} \frac{e^b - e^{-b}}{e^b + e^{-b}}$$

where r_{in} is the inner pipe radius of the heat pipe wall.

Lastly, the entrainment limit, also known as the flooding limit, can be obtained using a method proposed by Tien & Chung [51]. Entrainment would occur in a heat pipe along with flooding in the countercurrent vapor-liquid systems. The characteristic length of a screen mesh wick heat pipe can be represented in one of two ways, as shown in Eq. (85) and Eq. (86).

$$z = r_{eff} - D_{wire} \quad (85)$$

$$z = r_{eff} \quad (86)$$

The characteristic length can be used to obtain the flooding limit using Eq. (87) if the tilt angle is positive and Eq. (88) if the heat pipe is in the horizontal position.

$$\dot{Q}_{flo} = C_k^2 \left(\frac{D_{in}}{z} \right)^{0.5} A_v h_{fg} (\rho_l^{-0.25} + \rho_v^{-0.25})^{-2} [g \sigma \sin(\theta) (\rho_l - \rho_v)]^{0.25} \quad (87)$$

$$\text{where: } C_k = \sqrt{3.2} \tanh(0.5Bo^{0.25}), Bo = D_{in} \left[\frac{g(\rho_l - \rho_v)}{\sigma} \right]^{0.5}$$

$$\dot{Q}_{flo} = C_k^2 A_v h_{fg} (\rho_l^{-0.25} + \rho_v^{-0.25})^{-2} [g \sigma (\rho_l - \rho_v)]^{0.25} \quad (88)$$

where Bo is the Bond number and C_k is a constant based on the Bond number.

4.1.8 Boiling Limit

The boiling limit would occur when vapor bubbles form inside the wick due to excessive radial heat flux at the evaporator. Heat pipe dry out, and therefore failure may occur if the bubbles continue growing. The boiling limit in a cylindrical heat pipe with uniform heat flux can be determined using Eq. (89) [41].

$$\dot{Q}_{boi} = \frac{2\pi L_e K_{eff} \Delta T_{cri}}{\ln \left(\frac{r_{in}}{r_v} \right)} \quad (89)$$

where ΔT_{cri} is the nucleation superheat or the temperature difference between the wall and saturated liquid. The superheat can be calculated from Eq. (90) as a function of saturated properties and wick design.

$$\Delta T_{cri} = \frac{2\sigma T_v}{h_{fg}\rho_v} \left(\frac{1}{r_b} - \frac{1}{r_{men}} \right) \quad (90)$$

where r_b and r_{men} are the effective radius of the vapor bubbles and the meniscus radius of the liquid-vapor interface, respectively. An alternative method to calculating the boiling limit was presented by Faghri [41], which uses r_b and K_{eff} values from a screen mesh wick to calculate the nucleation superheat equation. The r_{men} value is taken to be equal to the wick effective pore radius, r_{eff} . A similar method to Faghri was proposed by Chi [43], except with a different r_b value was used. Lastly, a method was proposed by Reay & Kew [46], where the superheat is calculated using Eq. (91). This method is only applicable to plain surfaces.

$$\Delta T_{cri} = \frac{2\sigma T_v}{h_{fg}\rho_v} \left(\frac{1}{r_b} - \frac{1}{r_{men}} \right) \quad (91)$$

where δ_{tb} is the thickness of the thermal boundary layer and is approximated as the cavity diameter of the heat pipe wall, which has an average value of 2.5×10^{-5} m. This method proposed by Reay & Kew does not consider the wick type when obtaining the boiling limit.

4.2 Solution Procedure

The methods used to calculate each heat pipe operational limit are explained in this section using algorithms. An extensive literature survey was conducted to identify different models to obtain the heat pipe operational limits. This section shows that the results obtained using these models are sometimes quite different. Some of these methods were modeled as it was described in the literature. Modifications were made on some models to increase their accuracy through

iterations. In some cases, the model was not sufficiently explained, and thus the model had to be expanded using physical principles.

An overview of the overall numerical model is shown in Figure 19. The model begins by selecting the geometrical requirements of the heat pipe and wick structure. Heat pipe properties like mesh number, porosity, and permeability are first calculated. Then, the temperature loop begins. The temperature value changes in the model as the loop progresses. In the loop, the pipe operational limits such as capillary, sonic, and entrainment limits are determined using different methods.

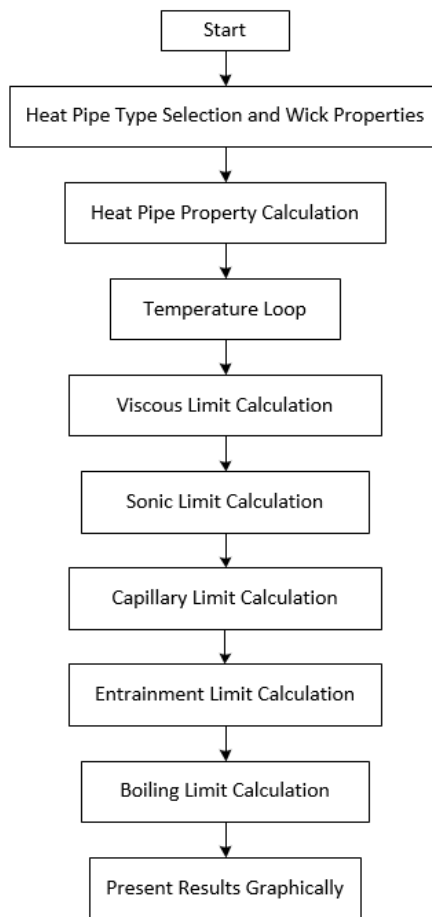


Figure 19: Numerical model algorithm.

4.2.1 Working Fluid Property Calculation

The saturated fluid correlations determine several different working fluid properties. These properties include pressure, density, latent heat, surface tension, thermal conductivity, specific heat ratio, etc. A property function is used in the model to determine a specific fluid property at a given temperature. The following is used to call the function “propertyFunction{#}(temperature),” where “#” represents the desired fluid property. The “temperature” is the given temperature in Kelvin. The “#” can be replaced with a number like “1”, which represents the saturated pressure,

or “10”, which means the vapor thermal conductivity. Using the temperature, the property value would be solved using the applicable polynomial correlation obtained from previous research [42].

4.2.2 Viscous Limit

Several approaches are used to solve the viscous limit using the equations introduced in Section 4.1. In total, there are five different methods that the model can use to determine the viscous limit. These methods will be explained below.

4.2.2.1 Busse Method 1, 2, and 3

The vapor channel area, A_v , vapor channel radius, r_v , evaporator exit temperature, $T_{evap,exit}$, constant, G (Eq.(54)), and effective length, L_{eff} , are all inputs used in the first technique. The stagnation temperature is defined to be the evaporator exit temperature. The saturation correlation is used to calculate the saturated pressure at the evaporator end, latent heat, and dynamic viscosity of the vapor from the vapor's isothermal temperature inside the evaporator. On the other hand, the ideal gas equation, Eq. (38), calculates the stagnation density using the evaporator temperature and pressure. The viscous limit is eventually calculated using Eq. (54). The steps needed to use this method when determining the viscosity limit are shown in Figure 20.

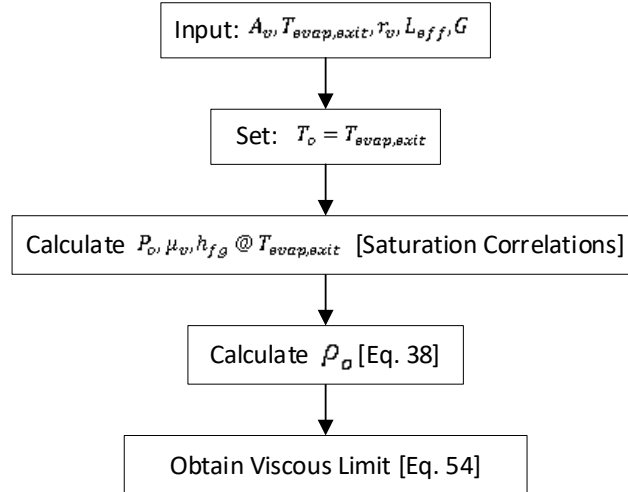


Figure 20: Busse option 1,2,3

The first method is similar to the second and third ways of getting the viscous limit. The second approach took a 10% pressure drop into account, whereas the third way took a 70% pressure drop into account. Equation (54) depicts the final equation used to calculate the viscous limit, where the constant G varied for the second and third methods.

4.2.2.2 Simple Iterative Method

The vapor radius, r_v , the evaporator exit temperature, T_{evap} , the adiabatic length, L_a , and the effective length, L_{eff} , were used as input parameters in the simple iterative technique. The saturation correlation code is used first to calculate the pressure, specific heat ratio, viscosity, sonic speed, latent heat, and vapor density from the vapor temperature at the evaporator outlet in order to determine the viscous limit at each particular temperature. The mass flow rate and velocity are then calculated based on a prediction for the viscous limit using Eq. (39) and (40), respectively. The Churchill friction factor and Reynolds number are then calculated using Eq. (46) and (47), respectively. To obtain a correct depiction of the Reynolds number, the friction factor is multiplied by the Reynolds number. Either Eq. (45) or Eq. (43) are used to get the compressibility factor and

Mach number, respectively. Equation (44) is used to determine the pressure drop in the evaporator portion. The MATLAB fsolve function is then used to calculate the viscous limit with a pressure drop equal to the pressure indicated by the saturation correlations.

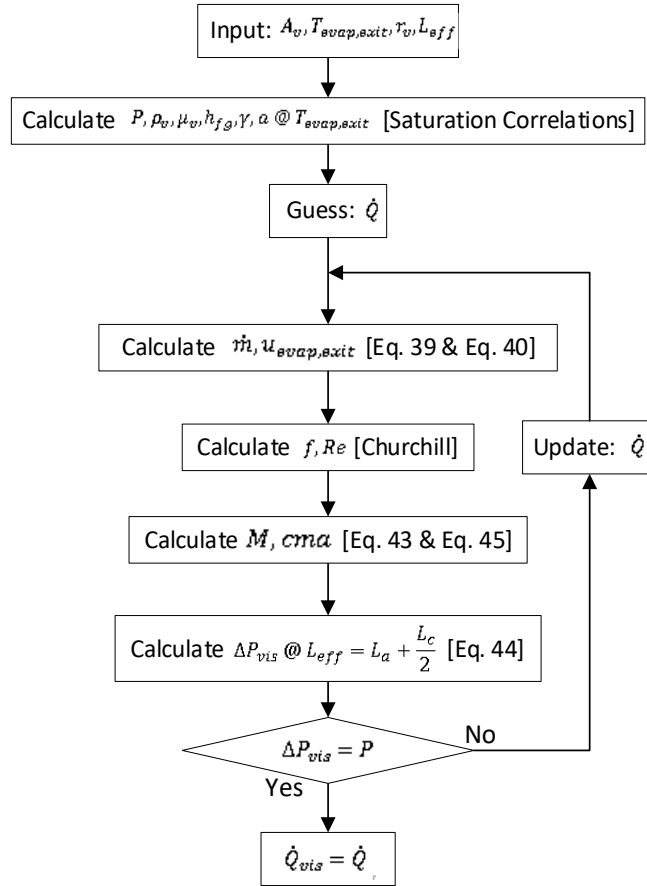


Figure 21: Simple iterative algorithm

4.2.2.3 Simple Iterative Method with Fanno Flow

The simple iterative algorithm with Fanno flow follows the same process as the simple iterative method. The viscous limit calculation is the only area of distinction. Figure 22 depicts an additional pressure drop. This pressure decrease from the adiabatic portion is calculated using the

equations presented in the Fanno flow section. The viscous limit is calculated using the MATLAB fsolve function after the pressure drops have been determined.

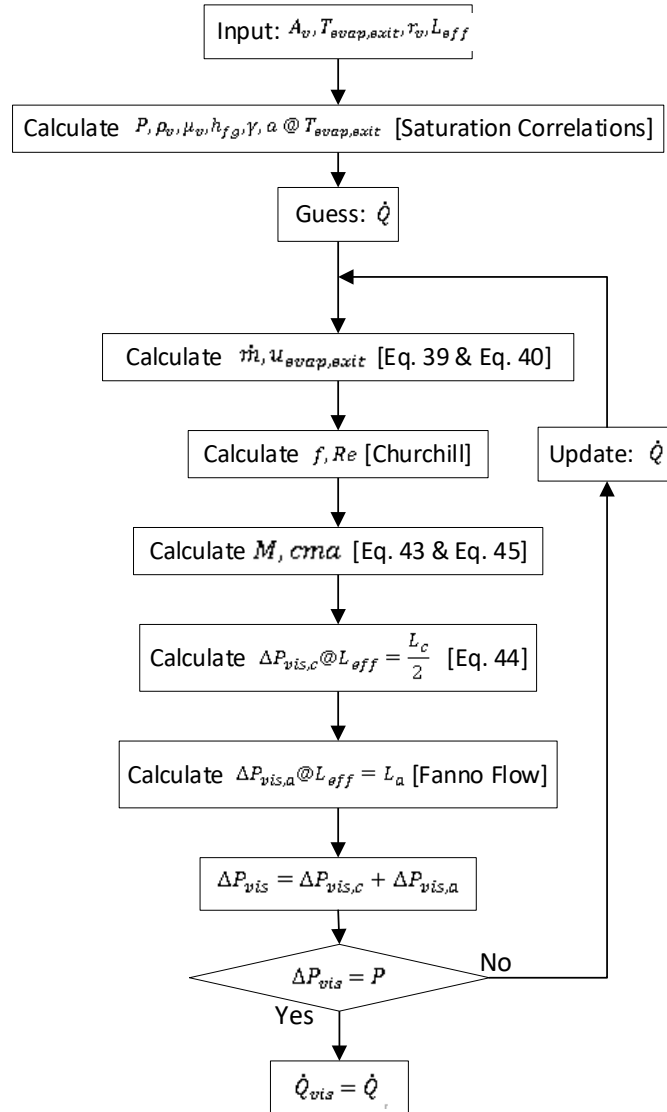


Figure 22: Simple iterative algorithm with Fanno flow

4.2.3 Sonic Limit

Numerous methods can be used to solve the equations stated in Section 4.1 to determine the sonic limit. Based on the equations in Section 4.1, seven distinct techniques were modeled.

4.2.3.1 Levy-stagnation Method

The vapor channel area, A_v , and the evaporator exit temperature, $T_{evap,exit}$, are input values for the Levy-stagnation method, as shown in Figure 23. Then, using Eq. (56), the stagnation temperature is determined. The saturation correlations are then used to calculate the stagnation pressure, sonic stagnation speed, specific heat ratio, and latent heat from the evaporator exit temperature. The ideal gas equation, Eq. (38), is used to determine the stagnation density. The sonic limit is calculated using Levy's equation, Eq. (55).

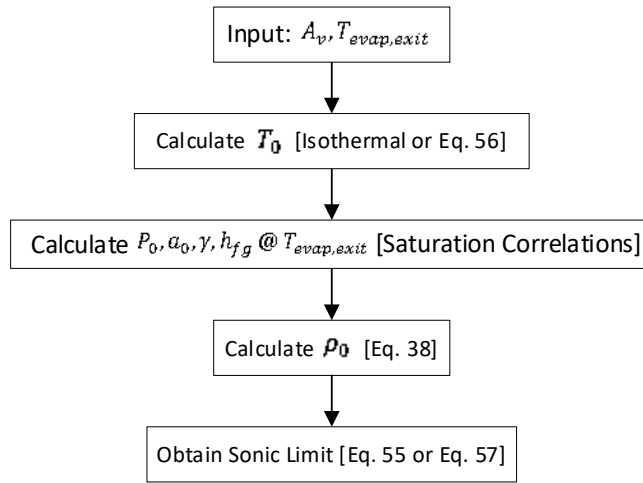


Figure 23: Levy methods and Busse method

4.2.3.2 Levy-isothermal Method

To determine the sonic limit, the Levy-isothermal approach introduced by Faghri can also be utilized [41]. For this method, Eq. (55) is employed, but the density is calculated using the isentropic sonic speed and assuming an isothermal evaporator.

4.2.3.3 Busse Method

Busse suggested a different approach that is similar to the one in Figure 23, where the sonic limit is calculated by using Eq. (57) rather than Eq. (55), and an isothermal evaporator assumption is used to get the stagnation temperature and sonic velocity.

4.2.3.4 Iterative Mach Number Method

Figure 24 depicts the iterative Mach number method. The input values for this approach are the vapor channel radius, r_v , adiabatic section length, L_a , and evaporator exit temperature, $T_{evap,exit}$. From the saturation correlations, the density, viscosity, specific heat ratio, sonic velocity, and latent heat are then determined. To calculate the velocity using Eq. (40), a guess of the Mach number at the evaporator outlet is taken. The Churchill equations (Eq. (46) and (47)) can then be used to compute the Fanning friction factor and the Reynolds number, respectively. The Fanno flow equations are then used to determine the Mach number at the condenser inlet. The mass flow rate is obtained using Eq. (40), and the sonic limit is derived using Eq. (39) only if the Mach number at the condenser input is equal to unity. If the Mach number is not equal to one, the evaporator exit Mach number is adjusted, and the procedure is repeated.

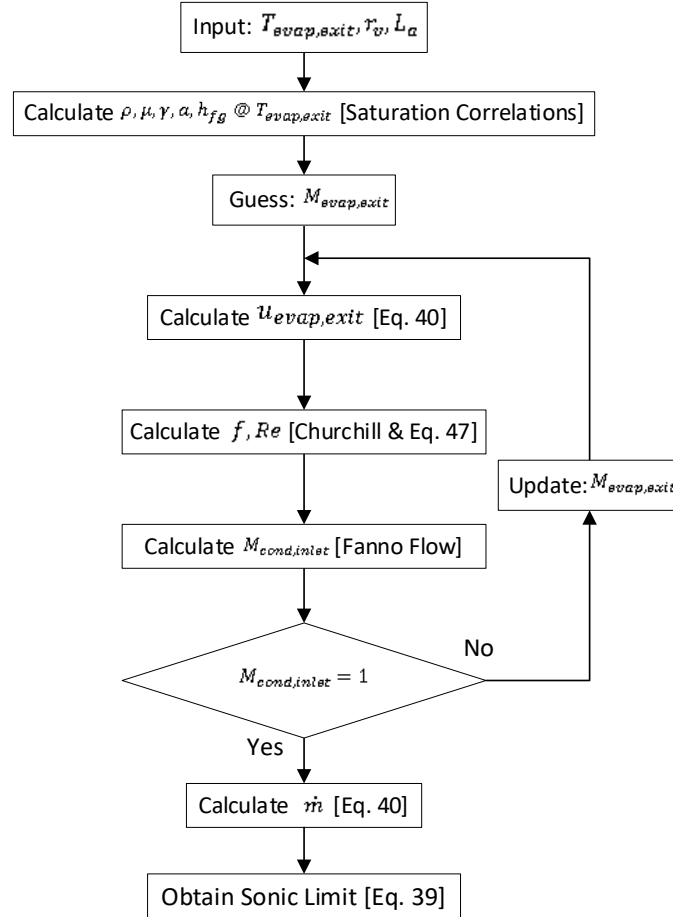


Figure 24: Iterative Mach number algorithm

4.2.3.5 Iterative Power Method 1

In Figure 25, an iterative power method is displayed. The input values for this approach are the vapor channel radius, r_v , vapour channel area, A_v , evaporator section length, L_e , and evaporator exit temperature, $T_{evap,exit}$. The saturation correlations are then used to calculate the pressure, density, viscosity, specific heat ratio, and latent heat. An initial estimation of the power is made. Then, using Eq. (39), the mass flow rate is determined. The Churchill correlation and Eq. (47) can then be used to compute the Fanning friction factor and the Reynolds number, respectively. The evaporator exit Mach number is set to 0.986 if the heat pipe does not have an adiabatic section.

On the other hand, if the adiabatic section is present, the Mach number at the evaporator exit can be calculated using the Fanno flow equations by assuming the Mach number at the condenser inlet is equal to one. Then, the evaporator exit velocity is determined using Eq. (40) and a velocity adjustment factor of 0.986. Using Eq. (61) and (62), the viscous pressure drop and the inertial pressure drop are determined. Then, using Eq. (60), one can determine the vapor pressure at the evaporator end. The stagnation temperature and stagnation pressure ratio are then determined using Eq. (56) and Eq. (59). The ideal gas equation and Eq. (38) are used to get the stagnation density. Once the new power has been determined, it is compared to the initial estimate using Eq. (58). The most recent power value is identified as the sonic limit if the power values converge. The initial power is updated, and the process is repeated if the power does not converge.

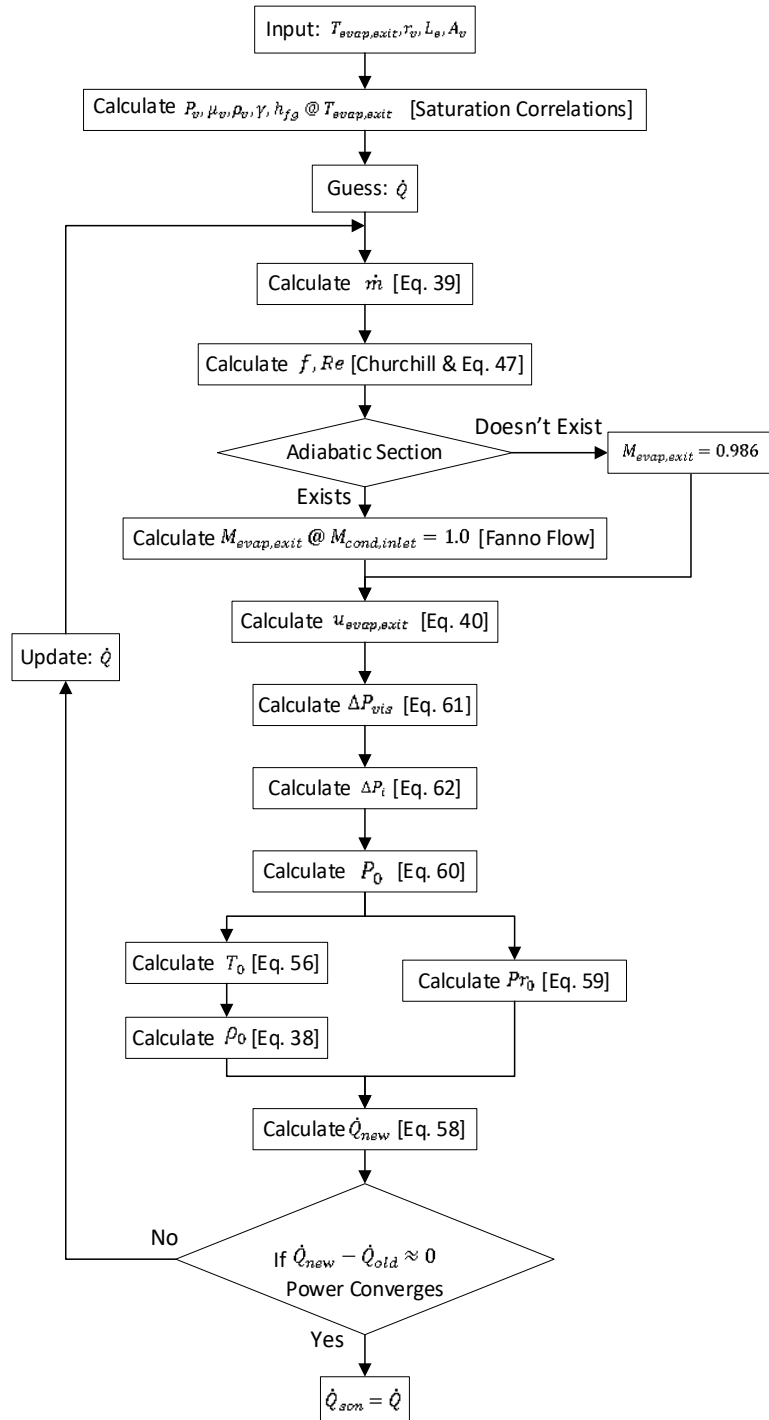


Figure 25: Iterative power method 1

4.2.3.6 Iterative Power Method 2

Figure 26 displays an iterative power method that is comparable to the one previously described. The input values for this approach are the vapor channel radius, r_v , vapour channel area, A_v , evaporator section length, L_e , and evaporator exit temperature, $T_{evap,exit}$. The saturation correlations are then used to calculate the pressure, density, viscosity, specific heat ratio, and latent heat. An initial estimate of the power is made. Then, using Eq. (39), the mass flow rate is determined. Then, using Eq. (46) and (47), the Fanning friction factor and the Reynolds number can be determined. The evaporator exit Mach number is set to 0.986, and the pressure ratio is set to unity if there is no adiabatic section in the heat pipe. The Fanno flow equations are used to determine the pressure ratio at the condenser inlet when its Mach number is unity and the adiabatic section is present. Then, using Eq. (63), the stagnation pressure at the evaporator end is determined. Using Eq. (38) and the saturation correlations, the stagnation pressure is utilized to get the stagnation temperature and the stagnation pressure ratio. The ideal gas assumption and Eq. (38) are used to get the stagnation density. The new power is then estimated using Eq. (57), and the results are compared to the initial estimation. The most recent power value is identified as the sonic limit if the power values converge. The initial power is updated, and the process is repeated if the power does not converge.

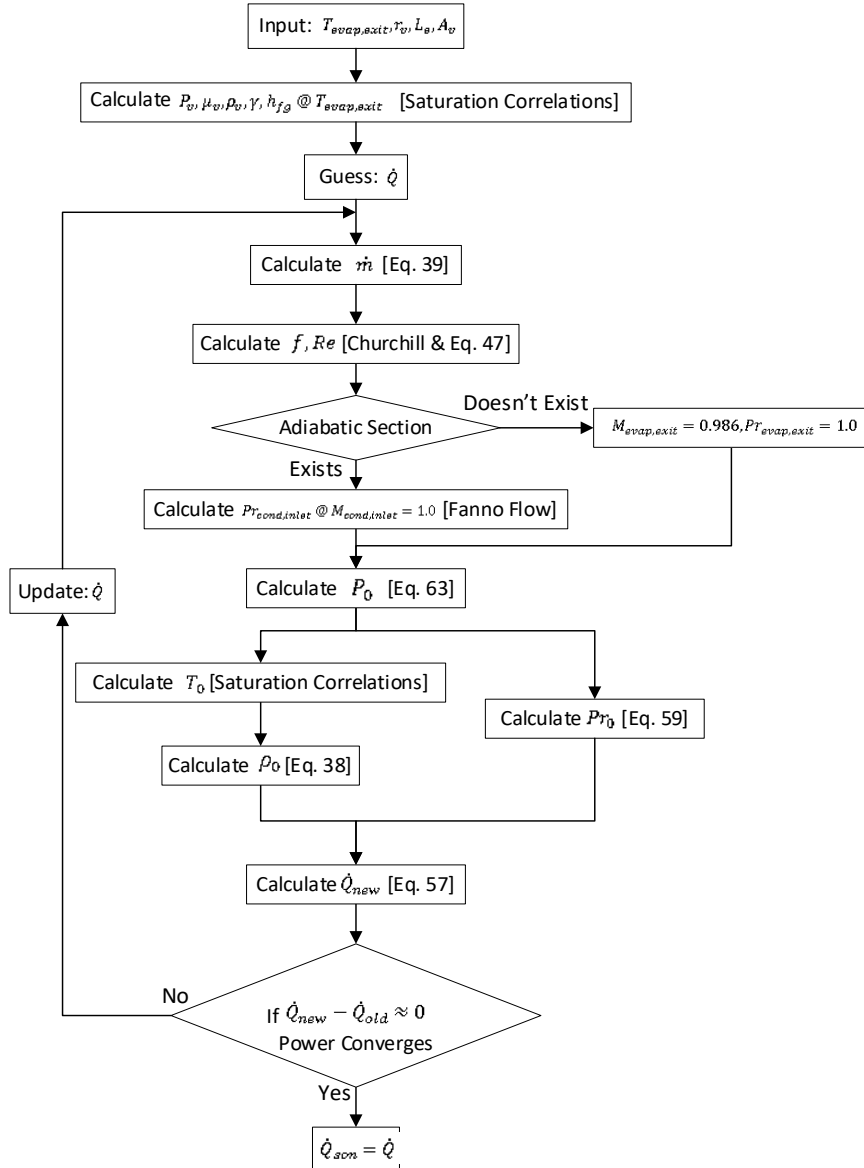


Figure 26: Iterative power method 2

4.2.3.7 Iterative Power Method 3

Figure 27 depicts the final iterative power method. The input values for this approach are the vapor channel radius, r_v , vapour channel area, A_v , evaporator section length, L_e , and evaporator exit temperature, $T_{evap,exit}$. The saturation correlations are used to calculate the pressure, density, viscosity, specific heat ratio, and latent heat. An initial guess of the power is

made. Then, using Eq. (39), the mass flow rate is obtained. Then, using Eq. (46) and (47), the Fanning friction factor and the Reynolds number can be calculated. The evaporator exit Mach number is set to 0.986 if the heat pipe does not have an adiabatic section. If the adiabatic section does exist, the Mach number at the evaporator exit can be calculated using the Fanno flow equations, presuming the Mach number at the condenser input is equal to one. Equations (64), (65), (66), and (67) can be simultaneously solved, yielding the stagnation pressure ratio and constant A . The stagnation temperature is set to be the same as the evaporator exit temperature. Then, using the saturation correlations, the stagnation pressure is determined. The ideal gas assumption, the evaporator exit temperature, the evaporator vapor pressure, and Eq. (38) are used to get the stagnation density. Once the new power has been determined, using Eq. (58), it is compared to the initial estimate. If the power values converge, the latest power value is determined to be the sonic limit. If the power does not converge, the initial power is updated, and the process repeats.

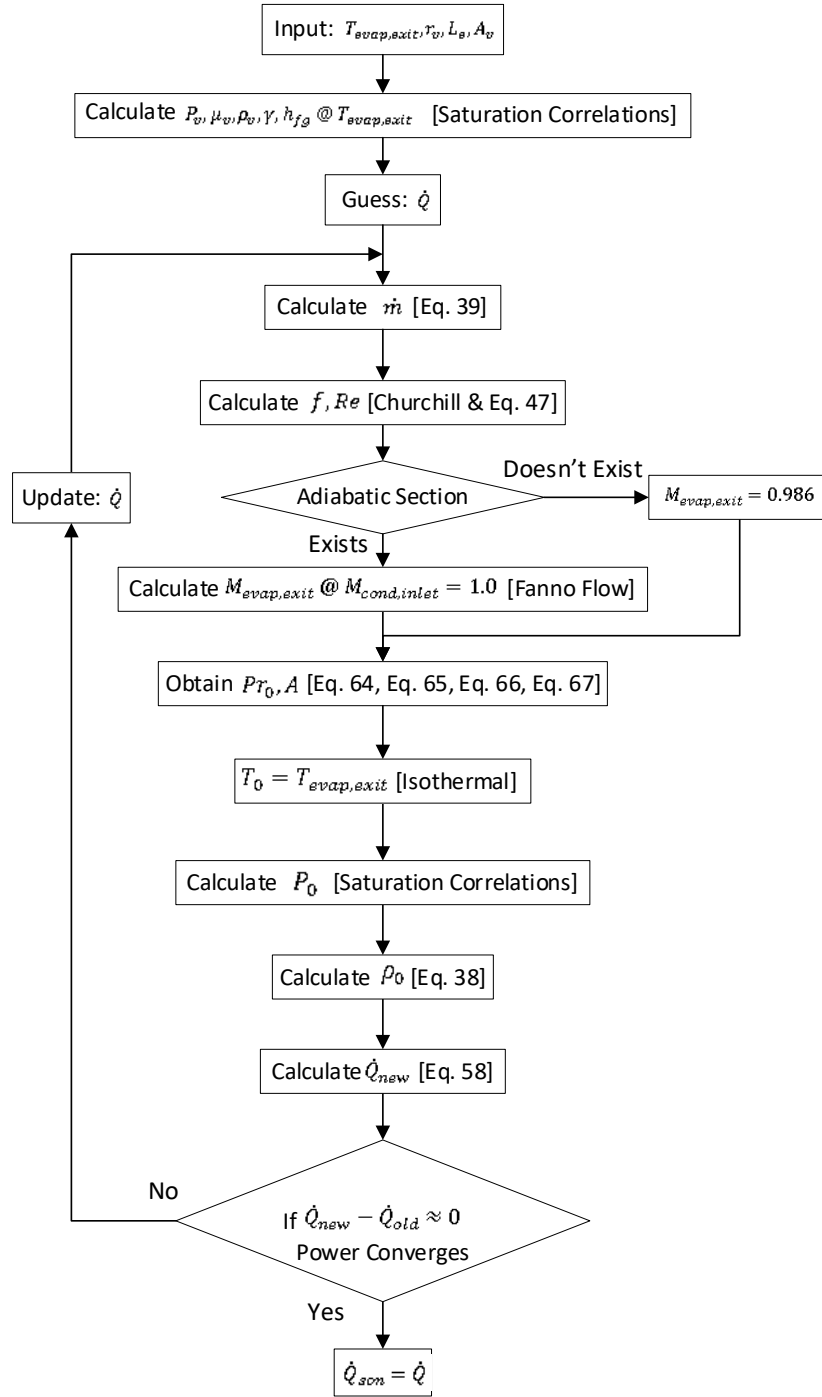


Figure 27: Iterative power method 3

4.2.4 Capillary Limit

Various methods can be used to solve the equations stated in Section 4.1 to calculate the capillary limit. Based on the equations in Section 4.1, four distinct techniques were modeled.

4.2.4.1 Reay and Kew Method

The wick area, A_w , wick permeability, k , heat pipe length, L_{total} , condenser radius, r_c , tilt angle, θ , and evaporator exit temperature, $T_{evap,exit}$, are used as inputs in the first method. The evaporator exit temperature is used to calculate the liquid's density, surface tension, and dynamic viscosity using saturation correlations. Using Eq. (70), the mass flow rate can be calculated. The capillary limit is then calculated using the mass flow rate and Eq. (71).

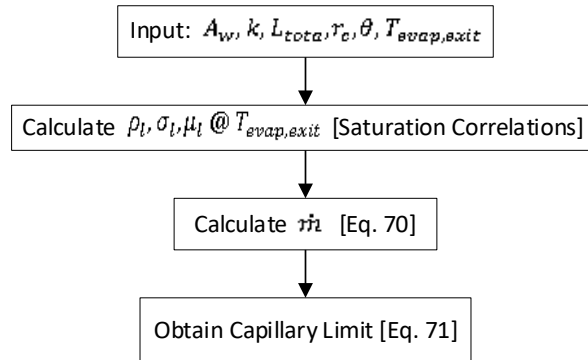


Figure 28: Reay & Kew algorithm

4.2.4.2 Simplified Chi Method

The simplified Chi method is another technique for figuring out the capillary limit. The input values for this method are the liquid and vapor areas, A_l and A_v , wick permeability, k , heat pipe length, L_{total} , effective radius, r_{eff} , vapor radius, r_v , tilt angle, θ , effective length, L_{eff} , and

evaporator exit temperature, $T_{evap,exit}$. Using the saturation correlations, the density and dynamic viscosity of the liquid and vapor and the latent heat are calculated. The liquid line's gravitational or tilt pressure change is determined using Eq. (53). Using Eq. (68), the capillary pressure is determined. To determine the capillary limit, the liquid pressure drop factor and the vapor pressure drop factor must be used. They can be found using Eq. (73) and Table 2, respectively. The capillary limit is then determined by applying these values to Eq. (72).

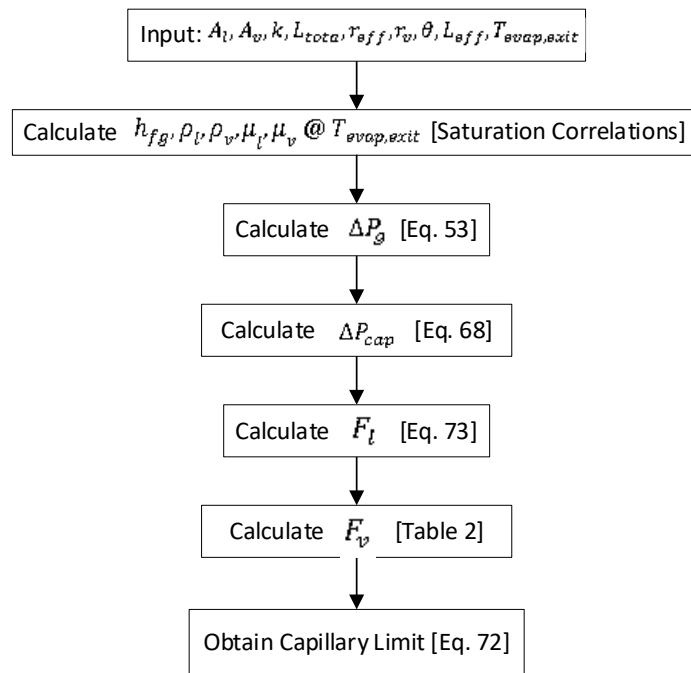


Figure 29: Simplified Chi algorithm

4.2.4.3 Chi Method

The evaporator exit temperature, $T_{evap,exit}$, the wick permeability, k , the heat pipe effective length, L_{eff} , the effective radius, r_{eff} , the vapor radius, r_v , the tilt angle, θ , the adiabatic length, L_a , the condenser length, L_c , and the liquid area, A_l , are all input values used in the non-simplified Chi method. The saturation correlations are used to calculate the density and dynamic

viscosity of the liquid and vapor as well as the latent heat, surface tension, specific heat, and sonic speed from the evaporator exit temperature. Equations (39) and (40) are used to calculate the mass flow rate and evaporator exit velocity based on an initial guess for the supplied power. Equations (47) and (43) are used to calculate the Reynolds number and the Mach number. The liquid and vapor pressure factors are then determined using Eq. (73) and Table 2. The liquid line's gravitational or tilt pressure change is determined using Eq. (53). Using Eq. (68), the capillary pressure is determined. These numbers are then employed in Eq. (72), where they are used to calculate the capillary limit and compare it to the initial power estimate. The power value is updated, and the loop would repeat if they do not converge. The most recent power value would be the capillary limit when the convergence is attained.

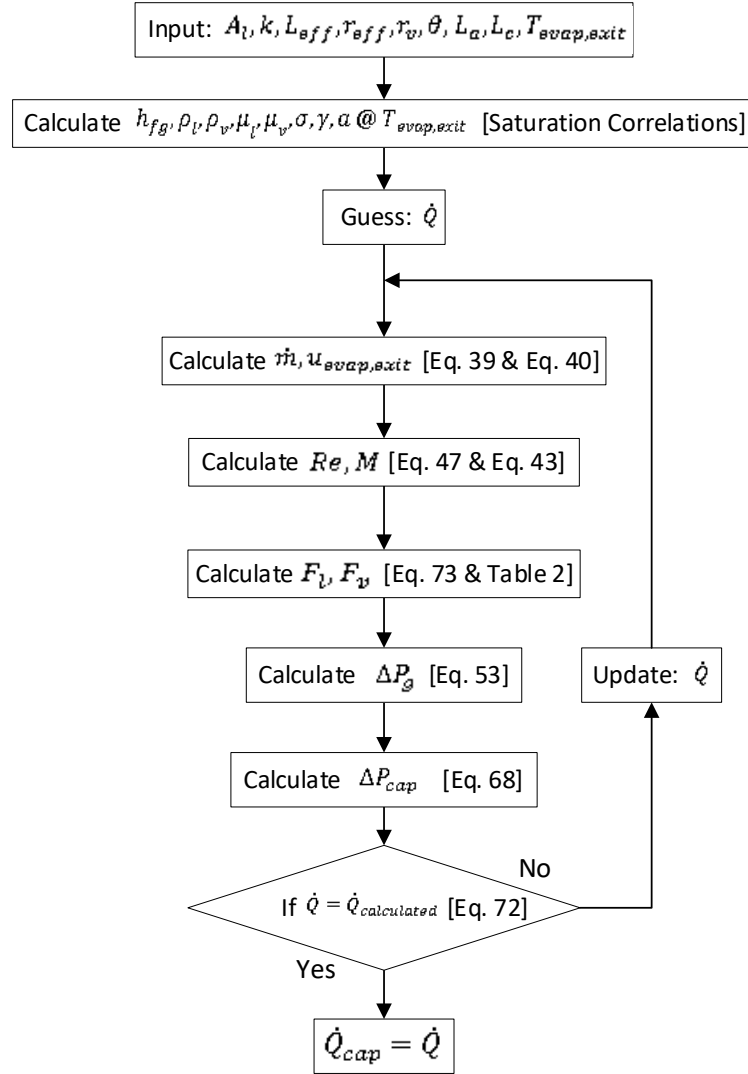


Figure 30: Chi algorithm

4.2.4.4 Iterative Pressure Method

The liquid area, A_l , wick permeability, k , heat pipe effective length, L_{eff} , effective radius, r_{eff} , vapor radius, r_v , tilt angle, θ , adiabatic length, L_a , condenser length, L_c , total heat pipe length, L_{total} , and evaporator exit temperature, $T_{evap,exit}$ are all inputs used in the iterative pressure method. The saturation correlations are used to calculate the density and dynamic viscosity of the

liquid and vapor as well as the latent heat, surface tension, specific heat, sonic speed, and vapor pressure from the evaporator exit temperature. In order to calculate the mass flow rate using Eq. (39), a first guess for the applied power is made. Using Eq. (68), the capillary pressure is determined. Eq. (75) is used to determine the vapor pressure drop in the evaporator. At the same time, the Fanno flow equations are used to determine the pressure decrease in the adiabatic region. Using Eq. (77), the condenser pressure drop is computed. The liquid line's gravitational or tilt pressure change is determined using Eq. (53). The total pressure loss is then calculated using these numbers in Eq. (69). The power value would update, and the loop would repeat if the capillary pressure and total pressure do not converge. The most recent power value would be the capillary limit when the convergence is attained.

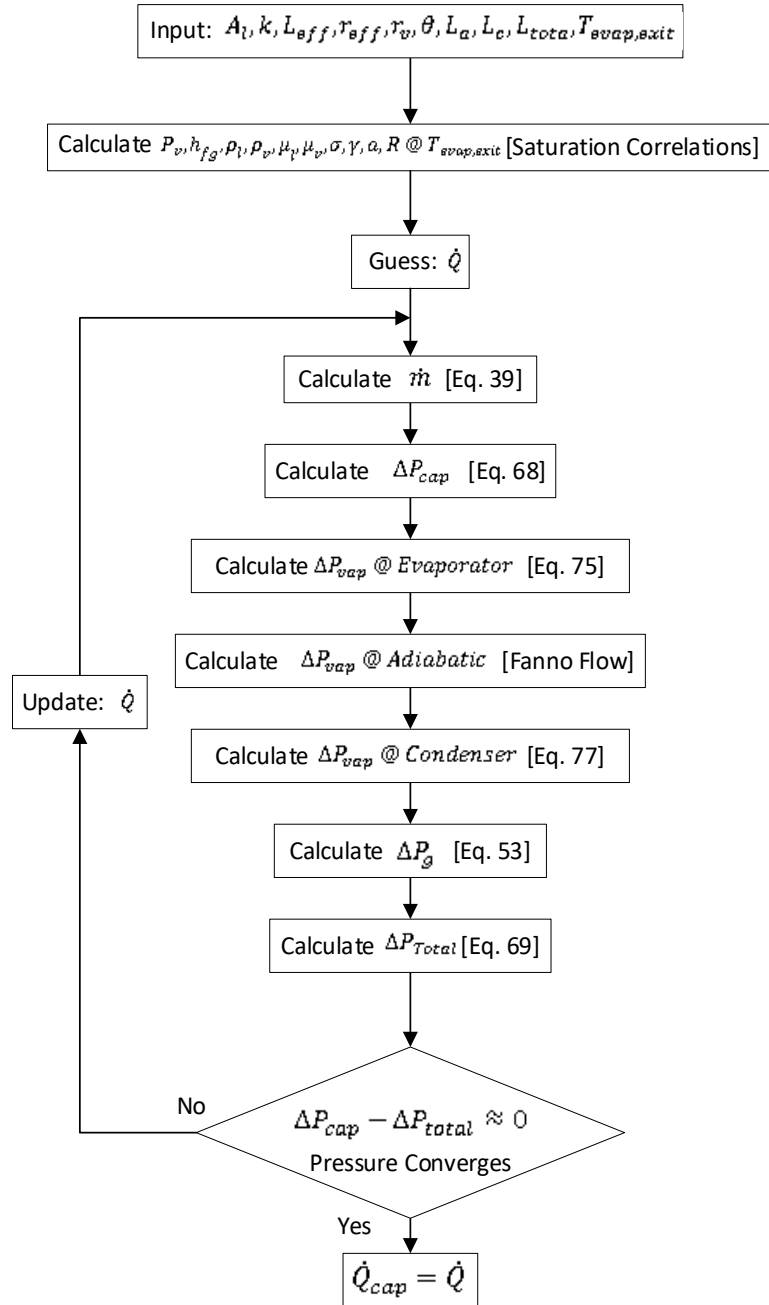


Figure 31: Iterative pressure method

4.2.5 Entrainment and Flooding Limit

To obtain the entrainment limit, several different methods can be implemented to solve the equations introduced in Section 4.1. In this work, six other methods were modeled based on the equations in Section 4.1.

4.2.5.1 Faghri, Sterbentz, Reay, and Kew Methods

The vapor channel area, A_v , the effective radius, r_{eff} , the wire radius, r_{wire} , and the evaporator exit temperature, $T_{evap,exit}$, are used as inputs in the first three methods. Calculating the length (z), which describes the liquid/vapor interface at the inner wick surface, is where the first three techniques differ. Faghri's technique uses Eq. (80) to calculate the length, z .

Equation (81) is used by the Sterbentz technique to calculate length z . The length, z , is determined by the Reay and Kew technique using Eq. (82). The surface tension, latent heat, and vapor density are computed from the vapor temperature at the evaporator outlet using the saturation correlations once the length value has been established. Following that, the entrainment limit is calculated using these values in Eq. (79).

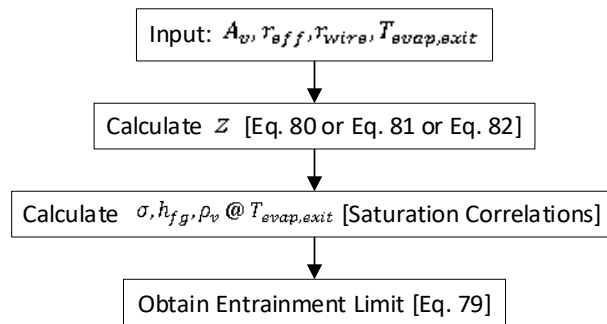


Figure 32: Faghri, Sterbentz, Reay & Kew algorithm

4.2.5.2 Prenger Method

The vapor channel area, A_v , the screen mesh depth, δ_w , the reference depth of the textured surface, δ_w^* , and the evaporator exit temperature, $T_{evap,exit}$, are the first inputs used in Prenger's approach. As previously noted, the reference depth, δ_w^* , is assumed to be 7.4×10^{-4} m, and the radius of the mesh wire is used as the depth of the screen mesh, δ_w . Using the saturation correlations, the surface tension, latent heat, and vapor density are determined from the vapor temperature at the evaporator exit. To determine the entrainment limit, Eq. (83) is used.

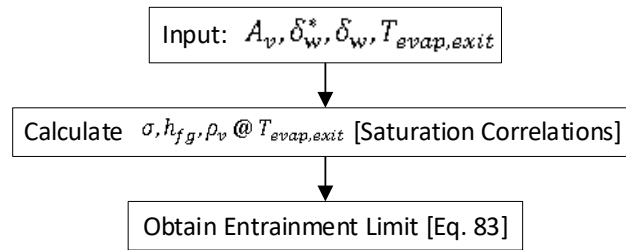


Figure 33: Prenger algorithm

4.2.5.3 Iterative Power Method

The vapor radius, r_v , the effective radius, r_{eff} , the wire radius, r_{wire} , the evaporator exit temperature, $T_{evap,exit}$, and the adiabatic length, L_a , are all input quantities used in the iterative power method. The length, z , is then calculated by dividing Eq. (80) by 4π . The saturation correlation code is used first to calculate the pressure, specific heat ratio, viscosity, speed of sound, surface tension, latent heat, and vapor density from the vapor temperature at the evaporator outlet in order to determine the entrainment limit at each particular temperature. The power loop then starts after this step and runs until the Weber number equals unity, at which point the loop ends. Using Eq. (39), the mass flow rate is calculated using the prediction for the entrainment limit. The

evaporator exit velocity is then calculated using Eq. (40). The saturation correlations and Fanno flow equations are used to calculate the condenser inlet velocity. The maximum velocity between the condenser inlet and evaporator exit is then selected. It is then used to determine if the Weber number has attained unity. If the value converges, the most current power value is set as the entrainment limit. The power value guess is updated, and the loop is repeated if the value does not converge.

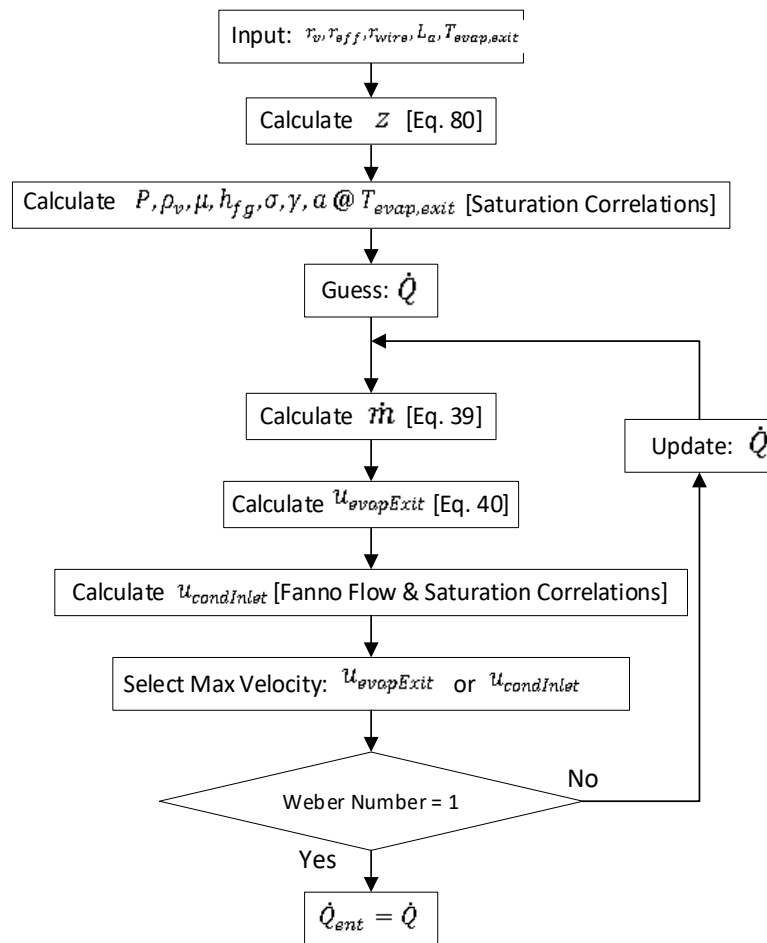


Figure 34: Iterative power method

4.2.5.4 Iterative Temperature Method

Using the saturation correlation code, the iterative temperature method first calculates the pressure, specific heat ratio, viscosity, speed of sound, surface tension, latent heat, and vapor density from the vapor temperature at the evaporator outlet. If the heat pipe's tilt angle is set to 90 degrees, the heat pipe will be in a vertical orientation. The entrainment limit is then calculated using Eq. (84). If the heat pipe is not vertical, the model would first use Eq. (82) to solve the length, z . The condenser inlet temperature is first estimated. Then, one of two techniques using Eq. (79) is used to find the entrainment limit. The entrainment limit is calculated using Eq. (79), and the initial density is calculated from the saturation correlations if an adiabatic section is absent. The density is calculated using the Fanno flow equations described in the Fanno flow section if an adiabatic section is provided. Eq. (78) is then used to determine the condenser inlet velocity while assuming a Weber number of one. The Fanno flow equations and the saturation correlations are used to determine the pressure, followed by the new condenser inlet temperature. If the new condenser inlet temperature converges with the initial guess value, the temperature loop ends. The updated density value and Eq. (78) are used to calculate the entrainment limit.

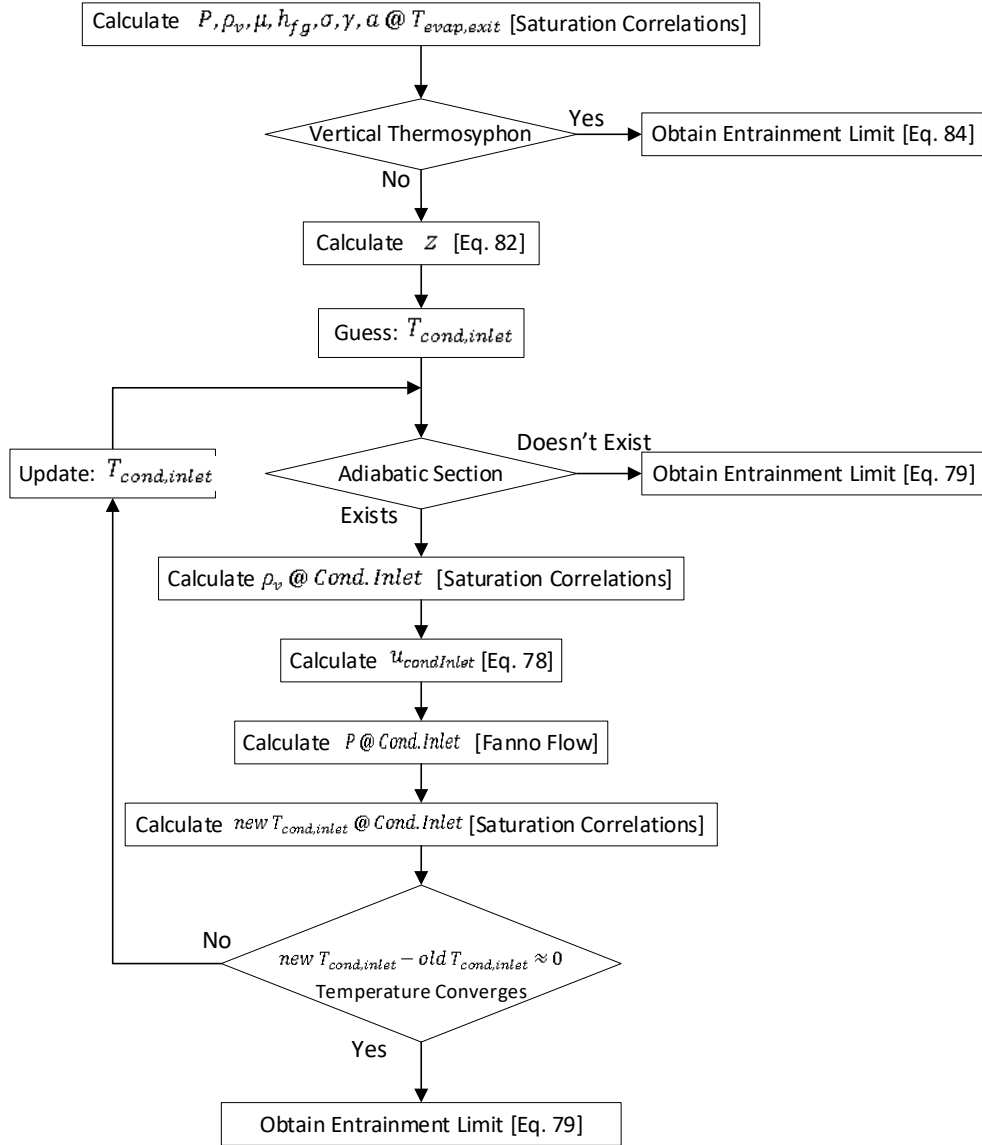


Figure 35: Iterative temperature method

4.2.5.5 Flooding Limit Method

The vapor channel area, A_v , the effective radius, r_{eff} , the wire radius, r_{wire} , the inner radius, r_{in} , the gravity acceleration, g , the tilt angle, θ , and the evaporator exit temperature, $T_{evap,exit}$, are used as input parameters to establish the flooding limit, as illustrated in Figure 36. Using the saturation correlations, the surface tension, latent heat, vapor density, and liquid density

are estimated from the vapor temperature at the evaporator exit. Using either Eq. (85) or Eq. (86), the characteristic length, z , is computed. If the heat pipe is horizontal, tilt angle is zero, the flooding limit is determined using Eq. (88). On the other hand, Eq. (87) is used to obtain the flooding limit if the tilt angle is greater than zero. The limit is not defined for a negative tilt angle.

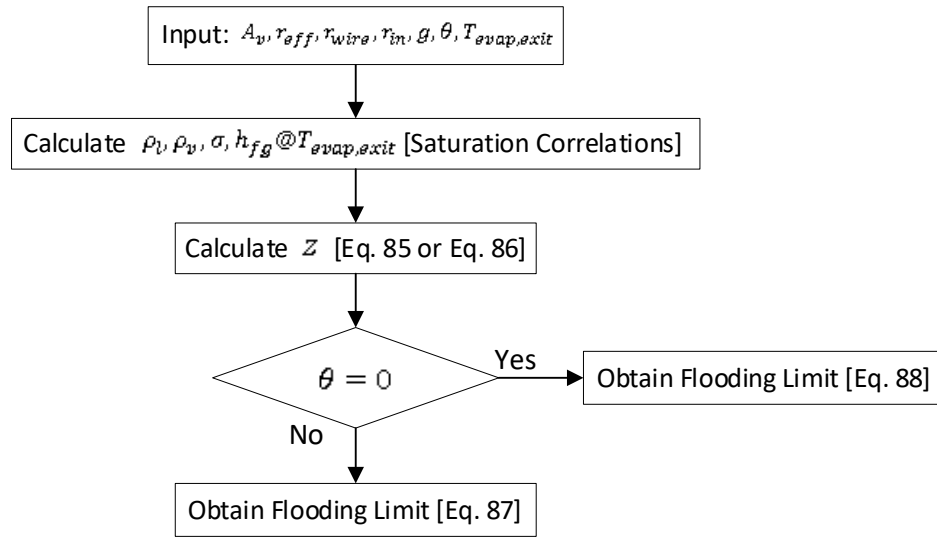


Figure 36: Flooding limit method

4.2.6 Boiling Limit

There are various methods that can be used to solve the equations stated in Section 4.1 in order to arrive at the boiling limit. Based on the equations in Section 4.1, three distinct techniques were modeled.

4.2.6.1 Faghri Method

The method used to estimate the boiling limit, as suggested by Faghri, is shown in Figure 37. The effective radius of the vapor bubbles, r_b , is specified in the numerical model to be 10^{-7} m, and the meniscus radius of the liquid-vapor interface, r_{men} , is assumed to be equal to the effective

pore radius of the wick, r_{eff} . K_{eff} , thermal conductivity is set depending on the wick type used. Using the saturation correlations, the surface tension, latent heat, and vapor density are determined from the vapor temperature at the evaporator exit. Equation (90) is then used to calculate the superheat. The boiling limit is then calculated using Eq. (89).

4.2.6.2 Alternate Faghri Method

A second version of the Faghri method is used to determine the boiling limit. The vapor bubbles' effective radius in this method, r_b , is set to 2.54×10^{-7} m. The liquid-vapor interface's meniscus radius, r_{men} , is calculated using the wick's effective pore radius, r_{eff} . The surface tension, latent heat, and vapor density are determined from the vapor temperature at the evaporator exit using the saturation correlations, as was discussed in the previous Faghri method. Equation (90) is used to calculate the superheat. Comparable to the previous Faghri method Eq. (89) is used to determine the boiling limit.

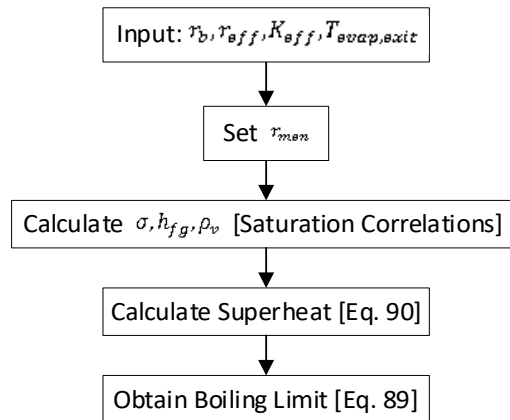


Figure 37: Faghri algorithm

4.2.6.3 Reay and Kew Method

The Reay & Kew method is the last technique. Figure 38 illustrates the precise steps involved in the Reay & Kew approach. The value of δ_{tb} , the thermal boundary layer thickness is set to 2.5×10^{-5} m. Using the saturation correlations, the surface tension, latent heat, and vapor density are determined from the vapor temperature at the evaporator exit. Then using Eq. (91) and the temperature values mentioned in the previous methods, the superheat is determined. The chosen wick type determines the value of K_{eff} . The boiling point is then determined by applying Eq. (89).

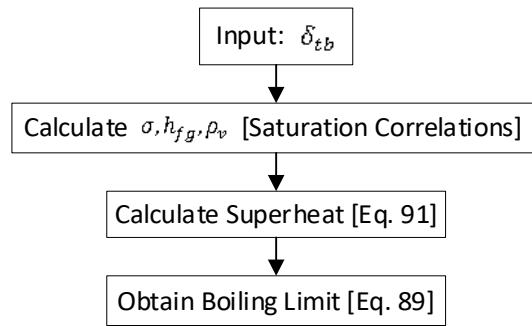
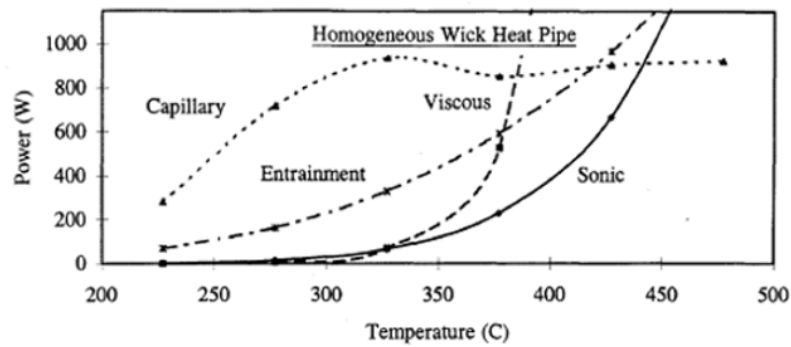


Figure 38: Reay & Kew algorithm

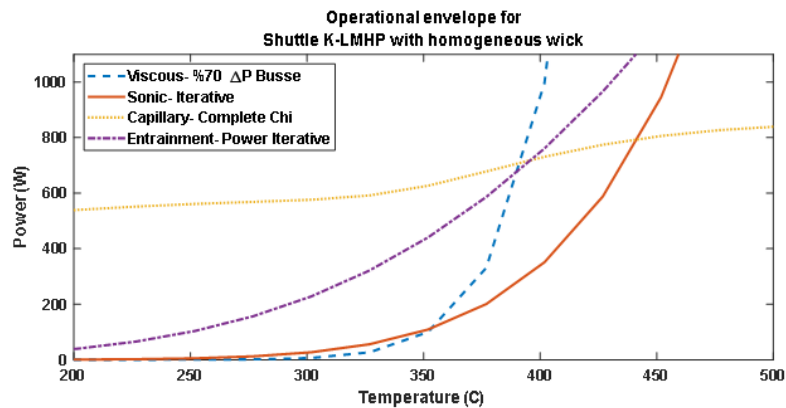
4.3 Results

The models were compared to the numerical results obtained by Dickinson [40]. This comparison can be seen in Figure 39. The top plot in the figure shows the viscous, sonic, capillary, entrainment, and boiling limits obtained by Dickinson, assuming a homogeneous wick heat pipe. The bottom plot shows the best-chosen operational envelope for a similar homogeneous wick heat pipe. The 70% of pressure Busse model (4.2.2.1) was chosen to be the best representation of the viscous limit. The iterative method (4.2.3.4) was selected as a good match for the sonic limit. The

capillary limit was best represented using the complete Chi method (4.2.4.3). The iterative power method (4.2.5.3) was selected to be the best for the entrainment limit. A detailed comparison to the previously published experimental results was not possible. This is due to insufficient information on the heat pipe characteristics and incomplete data sets. Experimental results are necessary to determine the best mathematical model for predicting liquid metal heat pipe operational characteristics. In the absence of the experimental results, the results were compared against Dickinson's work. These model results as shown in Figure 39 followed similar trends to Dickinson's results. The capillary limit showed the most variance, this may be due to insufficient information on the wick structure and wick permeability which impact the capillary limit.



(a)



(b)

Figure 39: Numerical model comparison (a) Dickinson model [40] (b) our model.

As some of the data on the heat pipe used by CNL for experimental testing were not accessible, numerous assumptions were made. The heat pipe would use liquid metal potassium as the working fluid. The orientation would be vertical, thus tilted 90 degrees. The length of the evaporator section was 0.125 m, the adiabatic section was 0.075 m, and the condenser section was 1.0 m. The outer diameter was 0.0254 m, and the wall thickness was 1.65 mm. The heat pipe was made of stainless steel and had a screen mesh wick. The possible operating temperature range for a heat pipe of this structure would be between 475 K and 1100 K. The operating limits of this heat pipe were investigated, and all the possible solution methods presented above in Section 4.2 were compared.

The five different viscous limits were compared in Figure 40. The Simple Iterative with Fanno Flow method was the most limiting option. Conversely, the first Busse method showed to be the least limiting method.

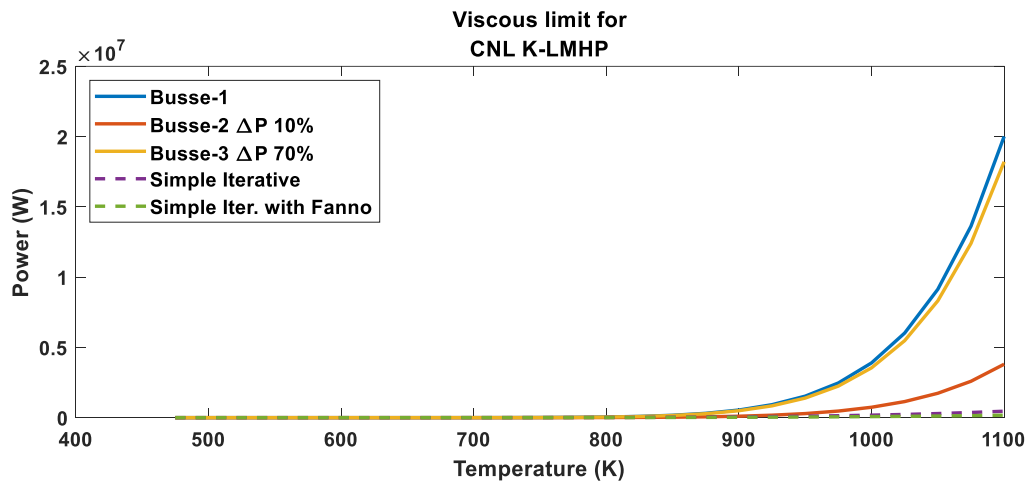


Figure 40: Viscous limit comparison.

The different sonic limit methods were compared to each other in Figure 41. In this figure, seven different methods were investigated, the Busse limit was the most limiting option, and the Iterative Power 1 method was the least limiting when considering the sonic limit.

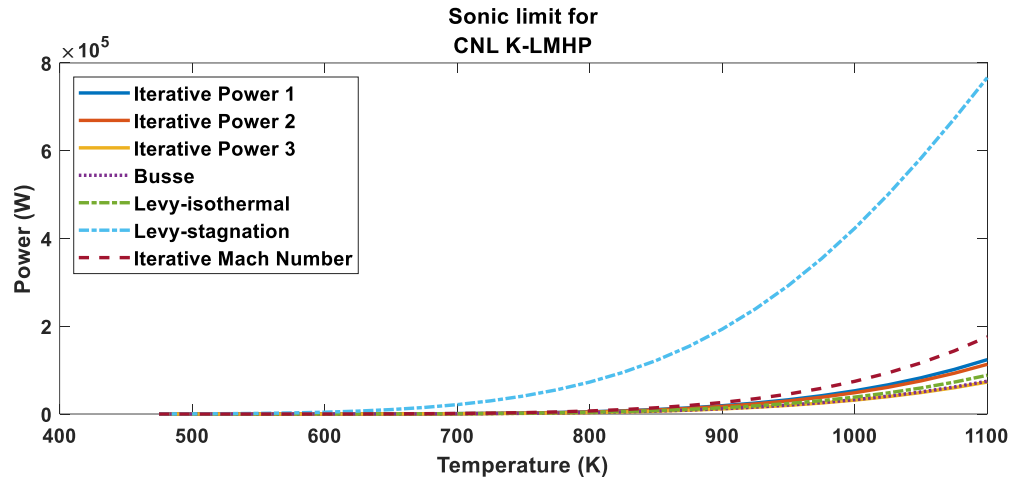


Figure 41: Sonic limit comparison.

Four different methods were investigated for the capillary limit. The Simplified Chi method was limiting at temperatures below 550 K. The Iterative Pressure method was the limiting method for temperatures between 550 K and about 675 K. Above 675 K, the Reay & Kew method was the limiting option. Similarly, at temperatures below 675 K, the Chi method was the least limiting method, and above 675 K the Simplified Chi method was the least limiting method of the four capillary limit solution methods.

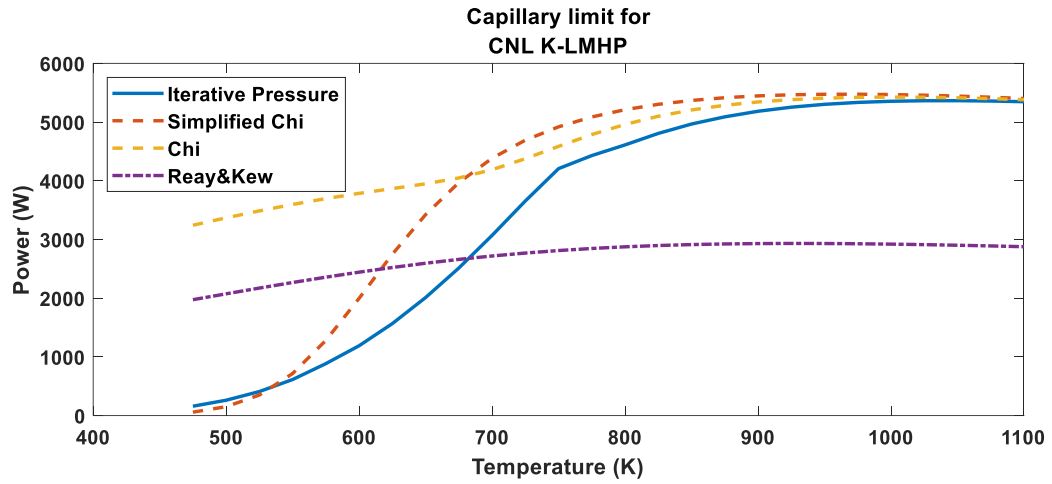


Figure 42: Capillary limit comparison.

Regarding the entrainment and flooding limit, seven different solution methods were investigated. The Prenger method was determined to be the most limiting option, and the Sterbentz method was found to be the least limiting when observing the different entrainment and flooding limits.

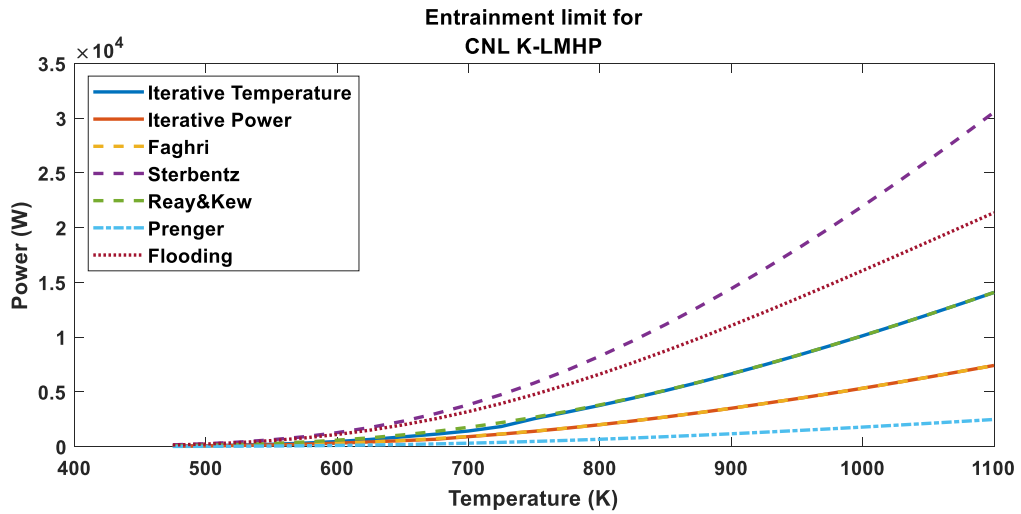


Figure 43: Entrainment limit comparison.

Lastly, the boiling limit was analyzed. Three different methods were compared. The Reay & Kew method was determined to be the most limiting method, and the Faghri method was found to be the least limiting. It is important to note that the boiling limit becomes more critical as the temperature increases.

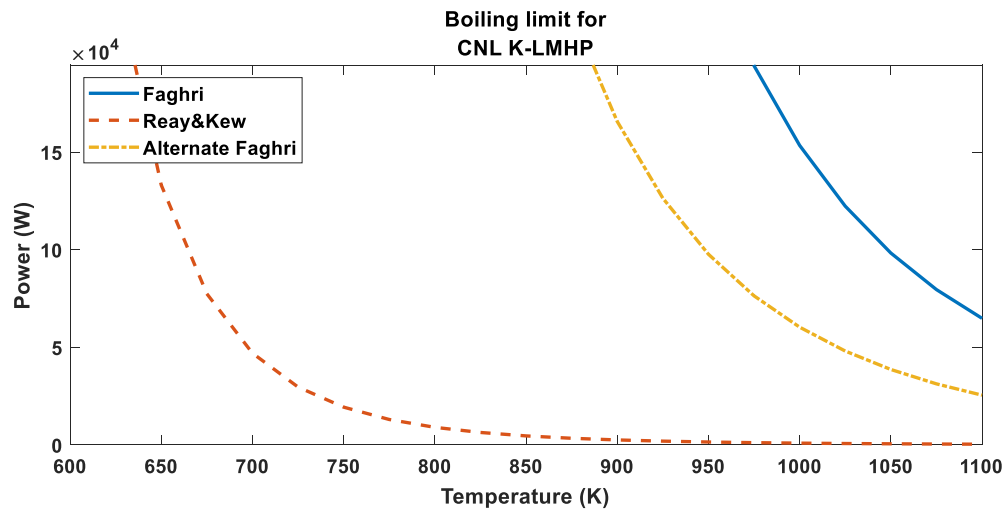


Figure 44: Boiling limit comparison.

The calculation of the operational envelope is crucial for nuclear applications. If one of these limits is reached during the operation, it may result in a severe accident such as core melt. An example of the heat pipe operation envelope is shown in Figure 45, considering all possible operational limits. At the time of writing this thesis, the expected data from CNL was not available to validate the operational envelope presented in Figure 45. The Busse 2 method, sonic iterative power 2 method, capillary iterative pressure method, entrainment iterative power method, flooding Tien and Chung method, and boiling alternate Faghri method were selected as they were found to be the most realistic in terms of physical conditions to that of CNLs experimental setup. The operational envelope was found using the lowest operating limit at the given temperature after applying a safety margin. The margin selected for the viscous and sonic limits was 50% of the

viscous and sonic limit, respectively. For the capillary, entrainment, and boiling limit margins, a value of 75% was used. The viscous and sonic limit methods were found to be less accurate based on previous research. Therefore, a more conservative margin value was applied when compared to the capillary, entrainment, and boiling limits. The minimum value of the operating limits after applying the margins was selected as the operating envelope value for the specific temperature.

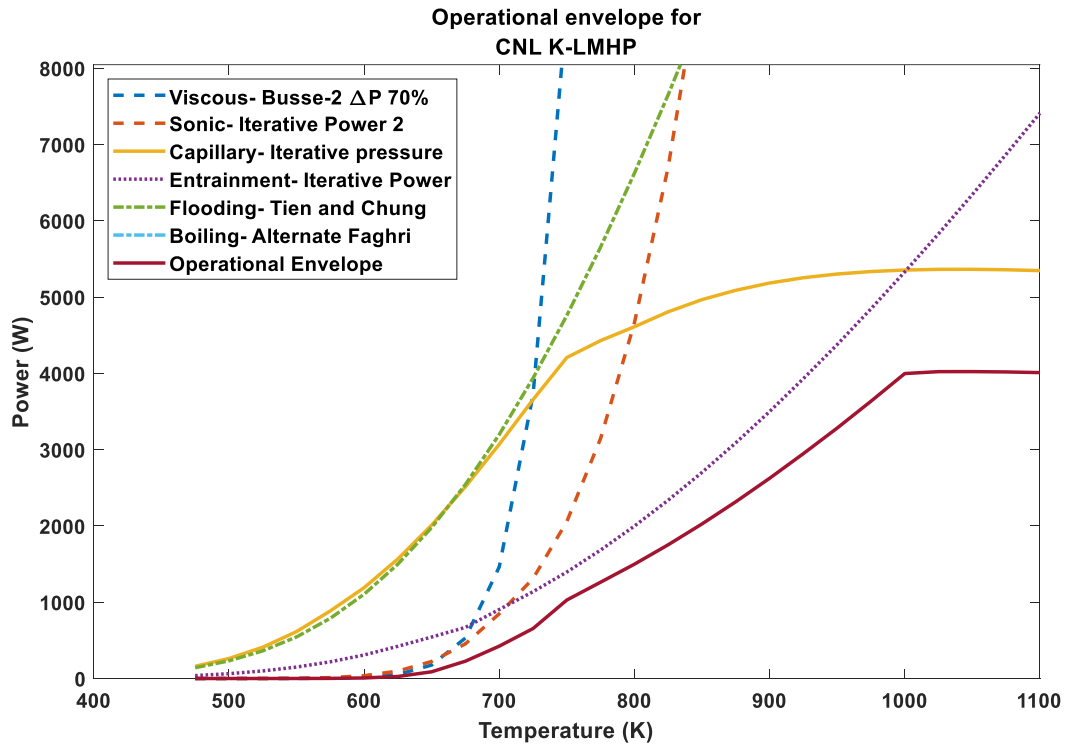


Figure 45: Operational envelope of possible CNL potassium heat pipe.

5 CHAPTER: Conclusions

A computer model was created to analyze molten metal flow in an empty vertical pipe and predict the penetration length. The one-dimensional numerical model included an adaptive time-step to account for the molten metal's rising velocity as it moved through the conduit. To monitor the pace of solidification and see if a complete blockage would occur, a thin solid layer was

modeled using a control volume technique. In order to account for the change in wall temperature as the molten metal would flow down the pipe, the wall was also modeled using a control volume technique. The model predicted the molten metal's penetration length using energy, momentum, and continuity equations. A previous analytical model that had been revised to forecast the length of penetration for a superheated liquid metal was used to validate the model. An experimental setup was created to test molten metal in a vertical pipe that was initially empty after going through various redesigns. The numerical model outperformed the analytical model in predicting the penetration length when it was compared to the experimental results. Overall, there was good agreement between the numerical code and the experimental results. The numerical model was updated for corium to better understand the flow of corium and potential blockage in vertical pipes. Overall, the concept of the melt flow plugging in vertical pipes as a passive safety factor in nuclear reactors was demonstrated. A numerical model was developed and validated to predict the penetration length.

Heat pipes were analyzed as a possible passive safety device for nuclear reactor core cooling and spent fuel pool cooling. A mathematical model for various heat pipe operating limits was presented together with a thorough explanation of the underlying ideas. The operational range of a typical liquid metal heat pipe was examined using various techniques. These operational restrictions include the sonic and viscous limits, which appear under low temperature working circumstances and may affect the heat pipe's capacity for heat transfer. It is possible for the entrainment, capillary, and boiling limits to occur under high-temperature working conditions. If these boundaries are crossed, the heat pipe may dry out, stopping the working fluid circulation and severely reducing the capacity for heat rejection. An extensive literature survey was conducted to identify different methods used to predict these limits. Some of these methods were further

extended to include a more accurate presentation of the actual physics. These operational limitations were programmed in MATLAB using the algorithms that were described. The techniques were then compared and analyzed. It was shown that there are severe discrepancies among these methods in predicting operational limits. To our best knowledge, this work was the first comprehensive analysis of the various proposed techniques. The outcomes of the numerical calculations were then contrasted with those shown in previous research. The results of these chosen methodologies appeared to follow comparable patterns to those found in the literature. The operational envelope for a typical liquid metal heat pipe was also presented. The calculation of this envelope is essential because if any of the operational limits are not respected, the heat pipe will fail, leading to a core meltdown.

5.1 Future Work

Some future work can be conducted on the melt flow solidification and the heat pipes. Regarding the melt flow solidification, the experimental design and numerical model can be enhanced in the future to improve the results. For instance, the wall and solid layer can get additional control volumes. The model would then mimic the temperature gradients more correctly with these additions. Surface tension can be included in the model for bigger pipe diameters to better reflect the flow's actual behavior. The numerical model would be more accurate in simulating the experimental flow if it considered the impacts of pressure transient waves that result from the solenoid valve opening. In the simulation, buoyancy effects weren't considered. Future work may incorporate the implications of buoyancy to depict the true nature of the flow more accurately. The accuracy of calculating the flow velocity could be enhanced by using a camera with a greater frame rate. Increased tube length between the solenoid valve and the cooling

reservoir would allow the gallium flow to develop fully before entering the cooling reservoir, which is another way to optimize the experimental setup. It is possible to simulate the pipes and flow that would occur in the CANDU reactor more accurately by using larger pipe diameters, various working fluids, and alternative pipe designs. To further describe the metal flow, 2D and 3D simulations can be carried out using a commercial CFD (Computational Fluid Dynamics) tool.

Future work for heat pipes can include model validation once the expected data from CNL is received. A more detailed and accurate operating envelope can be constructed using the different operating limit methods. Further experimental work can be done to understand how certain operating conditions can impact the function of liquid metal heat pipes and their operating limits.

Publications

The thesis led to three journal publications and one conference paper:

T. Beuthe, A. Vasic, H. Jazebizadeh, **A. Pegarkov**, T. Kaya, H. Zahlan, “Development of Analysis Tools for Heat Pipes Used in the Core Cooling of Small Modular Reactors: Potassium Property Correlations”, ASME Journal of Nuclear Engineering and Radiation Science, (Submitted March 2022)

A. Pegarkov, S. Somers-Neal, E. Matida, V. Tang, T. Kaya, “Experimental and Numerical Investigation of Solidification of Gallium in an Initially Emptied Vertical Pipe”, ANS Journal of Nuclear Science and Engineering, DOI: 10.1080/00295639.2022.2067738 (Online, May 2022)

A. Pegarkov, S. Somers-Neal, A. Alatrash, E. Matida, V. Tang and T. Kaya, “Numerical Investigation of Solidification of Corium in an Initially Emptied Vertical Turbulent Pipe Flow”, in 2021 International Conference on Mathematics and Computational Methods Applied to Nuclear Science and Engineering, Raleigh, North Carolina, USA.

S. Somers-Neal, **A. Pegarkov**, E. Matida, V. Tang, T. Kaya, “Experimental and Numerical Investigation of Solidification of Gallium in an Initially Emptied Horizontal Pipe Flow”, ASME Journal of Nuclear Engineering and Radiation Science, vol. 7, no. 3, 2021.

References

- [1] P. G. Martin, "The 2011 Fukushima Daiichi Nuclear Power Plant Accident: An Analysis from the Metre to the Nanometre Scale.," *Cham: Springer International Publishing*, 2019.

- [2] D. Jacquemain, *Nuclear Power Reactor Core Melt Accidents*, EDP Sciences, 2015.

- [3] W. Ma, Y. Yuan and B. R. Sehgal, "In-Vessel Melt Retention of Pressurized Water Reactors: Historical Review and Future Research Needs," *Engineering*, vol. 2, no. 1, pp. 103-111, 2016.

- [4] S. Somers-Neal, A. Pegarkov, E. Matida, V. Tang and T. Kaya, "Experimental and Numerical Investigation of Solidification of Gallium in an Initially Emptied Horizontal Pipe Flow," *Journal of Nuclear Engineering and Radiation Science*, vol. 7, no. 3, 2021.

- [5] B. Zohuri, *Heat Pipe Design and Technology: Modern Applications for Practical Thermal Management*, 2nd ed., Springer International Publishing, 2016.

- [6] INTERNATIONAL NUCLEAR SAFETY ADVISORY GROUP, "Basic Safety Principles for Nuclear Power Plants 75-INSAG-3 Rev. 1," INSAG Series No. 12, IAEA, Vienna, 1999.
- [7] M. Epstein, A. Yim and F. Cheung, "Freezing-controlled penetration of a saturated liquid into a cold tube," *Journal of Heat Transfer*, vol. 99, pp. 233-238, 1977.
- [8] F. Best, D. Wayne and C. Erdman, "A Fuel Freezing Model for Liquid-Metal Fast Breeder Reactor Hypothetical Core Disruptive Accidents," *Journal of Nuclear Science and Engineering*, vol. 89, pp. 49-60, 1985.
- [9] F. White, *Fluid Mechanics*, 7th ed., New York: McGraw-Hill, 2011, p. 366.
- [10] P. Sampson and R. Gibson, "A mathematical model of nozzle blockage by freezing," *International Journal of Heat and Mass Transfer*, vol. 24, no. 2, pp. 231-241, 1981.
- [11] P. Sampson and R. Gibson, "A mathematical model of nozzle blockage by freezing -II. Turbulent flow," *International Journal of Heat and Mass Transfer*, vol. 25, no. 1, pp. 119-126, 1982.

- [12] P. Sampson and R. Gibson, "Solidification of a liquid metal flowing through a circular pipe: a prediction of nozzle blockage," *Advances in Engineering Software*, vol. 3, no. 1, pp. 17-25, 1981.
- [13] M. A. Barron, C. Lopez and D. Y. Yedina, "Heat transfer and solidification of molten iron in a pipe," *Advances in Research*, vol. 2, no. 12, pp. 987-1002, 2014.
- [14] T. Nitheanandan and J. Choi, "Benchmarking severe accident computer codes for heavy water reactor applications," IAEA TECDOC No. 1727, Vienna, 2013.
- [15] S. Nijhawan, "Computer code ROSHNI's productions of CANDU severe accident progression and its confirmation of severity of reactor design omissions, source term vulnerabilities, and avoidable risks," in *Korean Nuclear Society Spring Meeting*, Jeju, Korea, 2019.
- [16] R. D. Zerkle and J. E. Sunderland, "The effect of liquid solidification in a tube upon laminar-flow heat transfer and pressure drop," *Journal of Heat Transfer*, vol. 90, pp. 183-190, 1968.
- [17] J. Spencer and A. D. Quastel, "Freezing Plug Formation in PHWR Calandria Vessel Penetrations," in *The 9th European Review Meeting on Severe Accident Research*, Prague, Czech Republic, 2019.

- [18] M. Mochizuki, T. Nguyen, R. Singh and T. Nguyen, "Heat Pipe Based Passive Emergency Core Cooling System For Safe Shutdown Of," *Applied Thermal Engineering*, 2014.
- [19] K. S. Kozier, "The nuclear battery: A very small reactor power supply for remote locations," *Energy*, vol. 16, no. 1, pp. 583-591, 1991.
- [20] D. I. Poston, "The Heatpipe-Operated Mars Exploration Reactor (HOMER)," *AIP Conference Proceedings*, vol. 552, no. 1, pp. 797-804, 2001.
- [21] A. Bushman et al., "The Martian Surface Reactor: An Advanced Nuclear Power Station for Manned Extraterrestrial Exploration," 2004.
- [22] I. V. Dulera and R. K. Sinha, "High temperature reactors," *Journal of Nuclear Materials*, vol. 383, no. 1-2, pp. 183-188, 2008.
- [23] C. Wang et al., "Transient behavior of the sodium–potassium alloy heat pipe in passive residual heat," *Progress in Nuclear Energy*, vol. 68, pp. 142-152, 2013.
- [24] M. S. El-Genk and L. M. Palomino, "SLIMM-Scalable LIquid Metal cooled small Modular Reactor: Preliminary design and performance analyses," *Progress in Nuclear Energy*, vol. 85, pp. 56-70, 2015.

- [25] J. W. Sterbentz et al., "Preliminary Assessment of Two Alternative Core Design Concepts for the Special Purpose Reactor," Idaho National Lab, Idaho Falls, ID (United States), 2017.
- [26] C. Yao, S. Zhao, G. Hu, J. Xie, J. Guo and J. Gao, "Scheme Research of Mars Surface Nuclear Reactor Power," in *The 20th Pacific Basin Nuclear Conference*, Singapore, 2017.
- [27] C. Mueller and P. Tsvetkov, "Novel design integration for advanced nuclear heat-pipe systems," *Annals of Nuclear Energy*, vol. 141, 2020.
- [28] J. Choi, C. Lim and H. Kim, "Fork-end heat pipe for passive air cooling of spent nuclear fuel pool," *Nuclear Engineering and Design*, vol. 374, 2021.
- [29] M. H. Kusuma, N. Putra, A. R. Antariksawan, R. A. Koestoer, S. Widodo, S. Ismarwanti and B. T. Verlambang, "Passive cooling system in a nuclear spent fuel pool using a vertical straight," *International Journal of Thermal Sciences*, vol. 126, pp. 162-171, 2018.
- [30] C. Lu, W. Cai, W. Ji, J. Yang, T. Wang, C. Cheng and H. Xiao, "Experimental and computational analysis of a passive containment cooling system with closed-loop

- heat pipe technology," *Atomwirtschaft. Internationale Zeitschrift für Kernenergie*, vol. 51, no. 29, pp. 280-286, 2020.
- [31] C. Ye, M. G. Zheng, M. L. Wang, R. H. Zhang and Z. Q. Xiong, "The design and simulation of a new spent fuel pool passive cooling," *Annals of Nuclear Energy*, vol. 58, pp. 124-131, 2013.
- [32] Z. Xiong, M. Wang, H. Gu and C. Ye, "Experimental study on the sub-atmospheric loop heat pipe passive cooling system for spent fuel pool," *Progress in Nuclear Energy*, vol. 79, pp. 40-47, 2015.
- [33] B. Sutharshan, M. Mutyala, R. P. Vijuk and A. Mishra, "The AP1000TM Reactor: Passive Safety and Modular Design," *Energy Procedia*, vol. 7, pp. 293-302, 2011.
- [34] INTERNATIONAL ATOMIC ENERGY AGENCY, "Design of Reactor Containment Systems for Nuclear Power Plants," IAEA Safety Standards Series No. NS-G-1.10, IAEA, Vienna, 2004.
- [35] U.S. DOE Nuclear Energy Research Advisory Committee, "A Technology Roadmap for," United States. Office of Nuclear Energy, Science, and Technology, 2002.

- [36] S. Somers-Neal, V. Nguyen, E. Matida, V. Tang and T. Kaya, "Unsteady Sensitivity Analysis of Corium Solidification in a Horizontal Pipe Flow," in *8th International Conference on Simulation Methods in Nuclear Science and Engineering*, Ottawa, 2018.
- [37] S. Somers-Neal, V. Nguyen, E. Matida, V. Tang and T. Kaya, "Sensitivity Analysis of Unsteady Corium Solidification in an Initially Emptied Horizontal Turbulent Pipe Flow," *Journal of Nuclear Engineering and Radiation Science*, vol. 6, no. 1, 2019.
- [38] S. W. Churchill, "Friction factor equation spans all fluid-flow regimes," *Chemical Engineering*, vol. 84, no. 24, pp. 94-95, 1977.
- [39] A. Malekpour and B. W. Karney, "Rapid Filling Analysis of Pipelines with Undulating Profiles by the Method of Characteristics," *ISRN Applied Mathematics*, vol. 2011, pp. 1-16, 2011.
- [40] T. J. Dickinson, "Performance Analysis of a Liquid Metal Heat Pipe Space Shuttle Experiment," 1996, p. 91.
- [41] A. Faghri, *Heat Pipe Science And Technology.*, Global Digital Press, 1995.

- [42] P. J. Brennan and E. J. Krociczek, "Heat Pipe Design Handbook: Volume II," NASA, NASA-CR-163662, 1979.
- [43] S. W. Chi, Heat pipe theory and practice: a sourcebook., New York: Washington : Hemisphere Pub. Corp., 1976.
- [44] S. W. Churchill, "Friction factor equation spans all fluid-flow regimes," *Chem Eng*, vol. 84, no. 24, pp. 94-95, 1977.
- [45] Y. A. Çengel and J. M. Cimbala, Fluid mechanics: fundamentals and applications., Boston: McGraw-HillHigher Education, 2006.
- [46] D. A. Reay and P. A. Kew, Heat pipes, 5 ed., Amsterdam: Elsevier, Butterworth-Heinemann, 2006.
- [47] C. A. Busse, "Theory of the ultimate heat transfer limit of cylindrical heat pipes," *International Journal of Heat and Mass Transfer*, vol. 16, no. 1, pp. 269-186, 1973.
- [48] P. Dussinger, Design and Testing of Titanium/Cesium and Titanium/Potassium Heat Pipes, 2004, p. 9.

- [49] J. W. Sterbentz, "Special Purpose Nuclear Reactor (5 MW) for Reliable Power at Remote Sites Assesment Report," Idaho National Lab, Idaho Falls, ID (United States), 2017.
- [50] F. C. Prenger and J. E. Kemme, "Performance Limits of Gravity-Assist Heat Pipes with Simple Wick Structures," *Advances in Heat Pipe Technology* , pp. 137-146, 1982.
- [51] C. L. Tien and K. S. Chung, "Entrainment Limits in Heat Pipes," *AIAAJ*, vol. 17, no. 6, pp. 643-646, 1979.